JOURNAL OF GEOPHYSICAL RESEARCH, VOL. 101, NO. D14, PAGES 19,043–19,060, AUGUST 27, 1996

Information on aerosol size distribution contained in solar reflected spectral radiances

D. Tanré and M. Herman

Laboratoire d'Optique Atmosphérique, Centre National de la Recherche Scientifique et Université des Sciences et Technologies de Lille, Villeneuve d'Ascq, France

Y. J. Kaufman

Laboratory for Atmospheres, NASA Goddard Space Flight Center, Greenbelt, Maryland

Abstract. Information on the aerosol size distribution contained in the reflected solar spectral radiances detected over the oceans can be reduced into two quantities. These quantities have been determined in an unbiased way with the use of the principal components. Consequently, only one to two parameters of the size distribution can be retrieved. For a single-mode distribution these parameters are the effective radius of the particles and the width of the size distribution. The accuracy of the retrieval depends on the view and illumination directions. Accurate knowledge of the refractive index, real and imaginary parts, is not critically important for the retrieval as long as the retrieved particles are smaller than 1.0 μm. An error budget shows that very clean conditions are not suitable for getting any information on the aerosol size distribution. A surprising result of this investigation is that the spectral reflectance of a bimodal-lognormal distribution can be simulated very well with spectral reflectance of a single lognormal with an appropriate radius and width of distribution, σ, that do not necessary correspond to an average of the bimodal values. The present results change drastically our philosophy regarding the retrieval scheme. Additional studies are needed to confirm the present results for nonspherical particles.

1. Introduction

Atmospheric aerosol has a significant impact on the Earth radiative budget [*Coakley and Cess*, 1985; *Joseph*, 1984; *Tanre et al.*, 1984; *Charlson et al.*, 1992] but because of the aerosol short lifetime and spatial variability it is difficult to assess this radiative forcing. *Hansen and Lacis* [1990] pointed out that as a result, one of the greatest uncertainties in climate modeling comes from uncertainty in the aerosol forcing. As aerosol particles interact with solar and terrestrial radiation, they perturb the radiative budget [*Liou et al.*, 1978; *Coakley et al.*, 1983]. Aerosol particles also serve as cloud condensation nuclei (CCN) or ice nuclei (IN) [*Twomey and Warner*, 1967; *Hobbs and Locatelli*, 1970; *Charlson et al.*, 1987; *Wigley*, 1989; *Hegg*, 1990] and therefore can modify cloud microphysic and radiative properties [*Twomey*, 1977a; *Twomey et al.*, 1984; *Albrecht*, 1989; *Coakley et al.*, 1987; *Radke et al.*, 1989; *Kaufman and Nakajima*, 1993]. The direct effect of aerosols on radiation and the indirect effect on cloud albedo may cause a cooling effect that can counteract a large part, or even all the present warming due to the increase in the CO_2 concentration [*Twomey et al.*, 1984; *Wigley*, 1989; *Kaufman et al.*, 1991; *Charlson et al.*, 1992; *Penner et al.*, 1992], but its estimation is very uncertain [*Intergovernmental Panel on Climate Change (IPCC)*, 1994].

Aerosols also play an important part in many biogeochemical cycles. Air-sea exchange of particulate matter contributes to the global cycles of aerosol particles [*Duce*, 1983]. Dimethylsulfide produced by phytoplankton [*Andreae and Barnard*, 1984] diffuses into the atmosphere and is oxidized to form SO_2 and then sulfate particles. Ocean water and sea salt are transferred to the atmosphere through air bubbles [*Heathershaw*, 1974; *Fairall et al.*, 1983; *Hoppel et al.*, 1990]. Biomass burning is an important source of organic particles, while the arid and semiarid regions are for mineral dust [*Prospero*, 1981; *Pye*, 1987]. Aerosols play also an important role in tropospheric chemistry by serving as a liquid phase that increases the speed of chemical reactions [*Crutzen*, 1983; *Taylor et al.*, 1983].

To fully understand the role of aerosol particles in atmospheric processes, their total content and characteristics (composition, size distribution) have to be monitored at a global scale. Because of their short lifetime (~ a week) and the corresponding high spatial and temporal variability, only a satellite approach can achieve this objective. Combining information sensed over the land and over the ocean is the ultimate goal, but the problem is very complex over land since the surface albedo is generally unknown. Algorithms have been developed over dense vegetation for which the albedo is very low in the blue and red bands [*Kaufman and Sendra*, 1988; *Holben et al.*, 1992]. Algorithms that assume that the surface is invariant have been used for multitemporal studies [*Fraser et al.*, 1984; *Tanré et al.*, 1988a; *Kaufman et al.*, 1990], but there is no simple way for getting the aerosol spectral information over land at a global scale. Therefore we concentrate in this work on oceans only.

The aerosol particle size is very important in assessing the aerosol climatic and biogenic impact. The small accumulation particles, e.g., sulfates or smoke from tropical biomass burning (effective radius $r_{\text{eff}} \approx 0.1 - 0.2$ μm [*Hoppel et al.*, 1990, *Hegg et al.*, 1993; *Artaxo et al.*, 1994]) have a different atmospheric

Paper number 96JD00333.
0148-0227/96/96JD-00333$09.00

and climatic role than maritime particles or dust. They are much more efficient (per unit mass) in scattering sunlight back to space or in modifying cloud microphysics and albedo.

Even inside the accumulation mode the size is critical. Sulfur can be oxidized to sulfate in the gas or liquid phase [*Hoppel et al.*, 1990]. In the gas phase it forms small particles ($r_{\text{eff}} \approx 0.1$ μm) that for the same sulfur mass are 8 times more effective in modifying cloud microphysics than sulfate particles formed inside clouds ($r_{\text{eff}} \approx 0.2$ μm). The fraction of sulfate generated in each phase is very uncertain (compare, for example, the global assessments of *Langner and Rodhe* [1991] with North Atlantic assessments of *Benkovitz et al.* [1994]), as is the dynamic interaction of sulfate and SO_2 with clouds [*Kaufman and Tanré*, 1994]. New evidence shows that due to difference in size, organic particles present in the same geographic regions where sulfur sources are located may affect clouds in a similar magnitude or even more than sulfates even though their mass concentration is significantly smaller [*Novakov and Penner*, 1993; *Rivera-Carpio et al.*, 1996]. Therefore it is very important to assess the ability of the new satellite systems to sense some of the size properties of aerosol.

Present satellite measurements are limited to reflectance measurements in one channel (from geostationary satellite like GOES or Meteosat) or two channels (from advanced very high resolution radiometer (AVHRR)/National Oceanic and Atmospheric Administration (NOAA), and algorithms can derive only the total aerosol content, assuming a given aerosol model. The aerosol model is taken from literature as the most representative one of the local conditions [*Shettle and Fenn*, 1979; *D'Almeida et al.*, 1991]. Such a method has been successfully applied over water [*Griggs*, 1975, 1979; *Mekler et al.*, 1977; *Koepke and Quenzel*, 1979] with a particular emphasis on Saharan dust studies [*Fraser*, 1976; *Carlson*, 1979; *Norton et al.*, 1980; *Dulac et al.*, 1992; *Jankowiak and Tanré*, 1992]. An operational global product is presently provided by NOAA from AVHRR data over oceans [*Rao et al.*, 1989]. A pioneer study has been performed from AVHRR/NOAA data by *Durkee* [1985] for deriving the aerosol model from the satellite image itself. *Kaufman et al.* [1990] and *Ferrare et al.* [1990] used an iterative technique to retrieve the aerosol particle size, single-scattering albedo, and optical thickness, simultaneously from AVHRR data over an adjacent land and ocean areas. The success of these attempts was limited due to the lack of good spectral resolution (only two bands), lack of adequate satellite calibration, and the presence of water vapor absorption. The next generation of satellite sensors will provide well-selected multispectral data; e.g., MODIS on the Earth Observing System [*Salomonson et al.*, 1989; *King et al.*, 1992], or multiangular data provided by POLDER on ADEOS [*Deschamps et al.*, 1994] and by MISR on EOS A [*Diner et al.*, 1989]. Polarized reflectances will be provided by POLDER and by EOSP [*Travis*, 1993]. While the polarized reflectance is sensitive to the particle refractive index [*Deuzé et al.*, 1993] and the directional reflectances to the optical thickness [*Martonchik and Diner*, 1992], it has been already demonstrated that the spectral dependence of the optical thickness carries out information on the aerosols size distribution [*King et al.*, 1978] and it can be reasonably expected that the spectral dependence of the satellite signal can be used in a similar way.

The present work is devoted to a theoretical assessment of the possibility of retrieving the aerosol characteristics from spectral radiances detected by MODIS over the water. To avoid atmospheric absorption, the MODIS channels used for aerosol retrieval were positioned in atmospheric windows [*Salomonson et al.*, 1989]. The mathematical principles of the retrieval scheme are given in section 2. To extract and quantify the information resulting from the use of the solar spectral information, we adopted the principal component analysis that is described in section 3. The range of the parameters we can expect to retrieve is described with the associated accuracy in section 4. Section 5 discusses additional problems, and section 6 concludes the paper.

2. Background

The mathematical approach of inversion schemes is briefly described and illustrated using the single-scattering approximation. It is based on radiances computed for a library of aerosol models and the MODIS spectral bands.

2.1. Theory

In radiative transfer, inverse problems applied to linear problems generally lead to the solution of the classical Fredholm integral equation of the first kind [*Twomey*, 1977b],

$$L(x) = \int_a^b K(x, y)n(y)\, dy \tag{1}$$

where $L(x)$ are the measurements, $K(x, y)$ are the kernels, $n(y)$ is the searched function, and a and b are the limits of the integral. As an example, retrieval of aerosol size distribution from spectral extinction measurements is based on (1) [*King et al.*, 1978]: x is the wavelength for which the measurement is performed, y is the radius of the particle, the kernels $K(x, y)$ are the extinction efficiency factors at the wavelength x (calculated from Mie theory as long as particles are spherical), and $n(y)$ is the size distribution. There are many other examples of inversion problems based on (1) like the inference of the vertical temperature profile from infrared measurements [*Chahine*, 1972], the retrieval of the ozone content from the scattered light in the ultraviolet region [*Mateer*, 1965], or like the retrieval of the size distribution from scattered light in the forward scattering directions near the Sun [*Twitty*, 1975; *Santer and Herman*, 1983].

This is exactly the problem we are facing for retrieving the size distribution from spectral reflectances: in (1), $L(x)$ are the reflectances measured in the spectral bands (noted x), the kernels $K(x, y)$ correspond to the radiance scattered in a spectral band x by particles whose size is noted y, and $n(y)$ is the size distribution. If the single-scattering approximation is valid and if the bottom boundary is nonreflecting, the reflectance at the top of the atmosphere (TOA) is given by

$$\rho_\lambda(\mu_s, \mu_v, \phi_v) = \frac{1}{4\mu_s\mu_v}\int_0^\infty \pi r^2 Q^s(m, r/\lambda)\, P(m, r/\lambda, \Theta)n(r)\, dr \tag{2}$$

where λ is the wavelength, Θ the scattering angle, μ_s and μ_v the cosine of the incident and observation angles, ϕ_v the difference azimuth angle, m the particle refractive index, and $n(r)$ the searched size distribution. The scattering coefficient $Q^s(m, r/\lambda)$ and the phase function $P(m, r/\lambda, \Theta)$ are derived

from Mie theory computations by assuming spherical particles [*Van de Hulst*, 1957].

Because there is too much correlation between the separate measurements, (1) is generally ill-conditioned and inversion may lead to unstable solutions, several methods were developed to overcome the difficulties. One can quote the constrained linear inversion method [*King*, 1982], the relaxation method [*Chahine*, 1972], statistical methods [*Rodgers*, 1976] or neural networks approach [*Ishimaru et al.*, 1990].

Instead of these classical inversion methods, an attractive alternative approach is the "lookup table" (LUT) approach. Radiative transfer calculations are precalculated for many values of the parameters, then results are compared with measurements until the best "fit" is obtained. This type of method is called the pseudoinversion method. The main shortcomings of such methods are (1) the database has to be very large for simulating all the possible conditions and (2) it is difficult to estimate the sensitivity of the aerosol inversion to the input parameters. There is also an additional problem that is the lack of uniqueness in the solutions, but this is a problem with all inversions. In the present study, as the spectral variation is known to be smooth, some channels may be correlated and this will help us to overcome the first shortcoming by reducing the database. There is a classical tool largely used in statistical methods to remove the intercorrelated observations and to extract the uncorrelated and independent variables called the principal component analysis (PCA). Such an approach could be very useful since, in addition, it will give us in an unbiased way the number of parameters that can be retrieved and thus will overcome the second shortcoming of the LUT approach.

2.2. Database

The remote sensing procedure is based on a database that should be representative of the possible range of aerosol models. As pointed out by *Whitby* [1978] and *Junge* [1963], an actual size distribution comes from the sum of single modes. To simplify the sensitivity study, the selected aerosol models have a single mode only. In section 5 it will be shown that there is an equivalency between the optical properties of a combination of several modes and a representative single mode.

From previous works we can reasonably assume that aerosol size distributions follow a lognormal distribution defined by

$$n(r) = \frac{dN(r)}{dr} = \frac{N}{(2\pi)^{1/2}\sigma 2.3r} \exp\left\{-\frac{(\log r - \log r_m)^2}{2\sigma^2}\right\} \tag{3}$$

where N is the density number, r_m the median radius, and σ the standard deviation of $\log r$.

The range of possible values for r_m and σ is taken from *d'Almeida et al.* [1991] who give in their Table 4.2 an overview of the variability of the aerosols properties,

$$0.001\ \mu\text{m} < r_m < 10.0\ \mu\text{m} \qquad \Delta \log r_m = 0.1 \tag{4}$$

$$0.20 < \sigma < 0.50 \qquad \Delta\sigma = 0.01$$

It covers the full radius range observed in maritime region [*Hoppel et al.*, 1990] of 0.03 and 0.10 μm for sulfate particles and 1 μm for the sea-salt particles, as well as the Saharan dust over the equatorial North Atlantic Ocean [*Jaenicke and Schütz*, 1978; *Prospero*, 1981], between 0.05 μm and several microns.

The aerosol composition depends on the origin of the aerosols. As a result, the range of possible refractive index values is quite large. Most of our study is performed with the following value:

$$m = m_r - in_i \tag{5}$$

where the real part m_r is equal to 1.45 and the imaginary part $n_i = 0.0$. For an additional sensitivity study we selected $1.55 \geq m_r \geq 1.40$ and $0.100 \geq n_i \geq 0.0$.

Computations of aerosol radiative properties have been performed for the MODIS spectral bands. The MODIS instrument has been described previously [*Salomonson et al.*, 1989; *King et al.*, 1992]. There are seven spectral bands that are potentially useful in the remote sensing of aerosols, two in the visible (0.470 to 0.555 μm), two in the near infrared (0.659 and 0.865 μm), and three in the short-wavelength/medium-wavelength infrared (1.240, 1.640, and 2.130 μm).

3. Principal Component Analysis

In this section we briefly review the principal component analysis, following by a discussion of the number of principal components needed to restore the spectral properties of the aerosol reflectances in the presence of radiometric noise of the MODIS instrument. We show that the relevant first two principal components can be represented by a combination of the spectral angstrom exponents.

3.1. Mathematical Description

Instead of using reflectance values, it is more relevant to work with quantities that are similar to angstrom coefficients since angstrom coefficients defined from the spectral optical thicknesses are, for instance, directly connected to the Junge parameter for a size distribution represented by a power law [*Junge*, 1963]. They are herein defined by

$$\alpha_\lambda(\mu_s, \mu_v, \phi_v) = \log\left\{\frac{\rho_\lambda(\mu_s, \mu_v, \phi_v)}{\rho_{865}(\mu_s, \mu_v, \phi_v)}\right\} \Big/ \log\left\{\frac{\lambda}{0.865}\right\} \tag{6}$$

where the reflectances are normalized to the reflectance at $\lambda = 865$ nm.

The $\alpha_\lambda(\mu_s, \mu_v, \phi_v)$ for a specific geometrical condition can be derived from the reflectance values given in (2). For a single-scattering approximation they are independent of the absolute value of τ_λ and only dependent on the spectral variation of τ and $P(m, r/\lambda, \Theta)$. They are used to construct a matrix **[α]** with a number **L** of columns that corresponds to the number of wavelengths λ and with a number **N** of rows that corresponds to the number of aerosol models. Each of the α_n^l elements is the α_λ value for the spectral band l and for the aerosol model n. Thirty-one values of σ and 41 values of r_m are used, so **N** = 1271 models are considered for one refractive index.

It is expected that some of the matrix elements are intercorrelated and less than the **N*L** elements are needed to rebuild the **[α]** matrix. The well-known technique for performing such a reduction in the data amount is the principal component analysis (PCA), also called sometimes the empirical orthogonal function (EOF).

Any **N*L** matrix with $N \geq L$ can be rewritten

$$\mathbf{[\alpha] = [A]\{\lambda\}[P]} \tag{7}$$

where **[A]** is a column-orthogonal matrix (same shape as **[α]**; that is, **N*L**), **[P]** is an orthogonal square matrix (**L*L**), and [λ] is a diagonal matrix (**L*L**). Eq (7) corresponds to a singular

Table 1. Characteristics of the MODIS Channels Used in the Present Study

Center Wavelength	$Ne\Delta L$	$Ne\Delta\rho$	Maximum Reflectance
470	0.145	2.35×10^{-4}	0.96
550	0.127	2.11×10^{-4}	0.86
659	0.169	3.39×10^{-4}	1.38
865	0.123	3.99×10^{-4}	0.92
1240	0.045	3.12×10^{-4}	0.47
1640	0.027	3.63×10^{-4}	0.94
2130	0.009	3.06×10^{-4}	0.75

value decomposition. The matrices **[A]** and **[P]** are orthogonal, which means

$$\mathbf{[A^t][A] = [P^t][P] = [I]} \tag{8}$$

with **[I]** the identity matrix.

From (7) and (8),

$$\mathbf{[\alpha^t][\alpha] = [P^t]\ \{\lambda\}^2\ [P]} \tag{9}$$

which means that P and λ^2 are the eigenvectors (or principal components) and the eigenvalues of **[α^t] [α]**. The eigenvalues are the variances of the projection of the points along each of the principal axes.

Matrix **[A]** is given by

$$\mathbf{[A] = [\alpha]1/\{\lambda\}^2\ [P]^{-1}} \tag{10}$$

[P] and [λ] are obtained by solving (9), **[A]** by solving (10); so each matrix element α_n^l of the matrix **[α]** can be written

$$[\alpha_n^l] \equiv \sum_{j=1}^{L} \lambda_j [A_n^j][P_l^j] \approx \sum_{j=1}^{K} \lambda_j [A_n^j]\ [P_l^j] \equiv \sum_{j=1}^{K} [p_n^j]\ [P_l^j] \tag{11}$$

where $[A_n^j]$ is a column matrix with **N** elements, $[P_l^j]$ is a row matrix with **L** elements, and K is the number of principal components. P_l^j are the principal components and p_n^j are the loadings of the nth model on the jth principal component. As the useful spectral information is contained in less spectral bands than the original L number, K values λ_j only are significant (equation (11)). This results in **K(N + L)** elements only, instead of **N*L** elements of the original matrix **[α]**. If the value of K in (11) is smaller than **N*L/(N + L)**, we clearly reconstruct the initial database with a "sufficient accuracy" but with less data amount (the notion of "sufficient accuracy" will be discussed below). The new coordinate system, by means of orthogonal transformation, gives us a set of uncorrelated components.

Finally, from the Mie theory the 6×1271 angstrom coefficients, i.e., the 6×1271 elements α_n^l, are computed according to (2) and (6). Then, the inversion scheme is applied using (9) and (10) and the principal components P_l^j and the loadings p_n^j are derived.

3.2. Number of Significant Components

How many components **K** are significant is the key point of the present study since it will define the number of parameters we can expect to retrieve. We selected typical observation conditions (that we call standard case in the next sections): the solar zenith angle is 45°, satellite observations are at nadir, and the refractive index of aerosols is 1.45-0.000**i**; similar results were obtained in other conditions. As already mentioned, the method is applied to MODIS and so we use the seven MODIS solar bands reported in Table 1. Note that in this section, for mathematical convenience, the computations are performed using the normalized angstrom coefficients (which gives an average of 0 and a variance of 1.0); that is,

$$\delta\alpha_\lambda = \frac{\alpha_\lambda - \langle\alpha_\lambda\rangle}{\sigma_\lambda} \tag{12}$$

where $\langle\alpha_\lambda\rangle$ is the mean value of the angstrom coefficient and σ_λ the standard deviation over the selected database.

The values of the eigenvalues for the selected data set are reported in Table 2. The table shows that most of the variance is given by the two first components and most of the spectral dependence is restored by these two components, so the problem is well conditioned since we have two input parameters. To confirm the ability of the two first components to restore the spectral information, we plotted in Figure 1 the normalized reflectances R_λ^{exact} coming from the single-scattering approximation and R_λ^{acp} given by

$$R_\lambda^i = \frac{\rho_\lambda^i(\mu_s, \mu_v, \phi_v)}{\rho_{865}^i(\mu_s, \mu_v, \phi_v)} \tag{13}$$

as a function of the wavelength, for several values of r_m and σ. For clarity the angular dependence is omitted. The reflectances $\rho_\lambda^{\text{acp}}$ have been computed by using the two first principal components. For all the standard deviations σ of the size distribution in Figure 1, 0.20, 0.35, and 0.50 (Figures 1a, 1b, 1c, respectively), the agreement is quite good for all the three values of r_m, 0.01, 0.10, and 1.00 μm. Differences between the exact normalized reflectances and the reflectances restored from the two first components are also reported in Table 3.

The "quality" of the restitution as a function of the number of the principal components, K, is defined by

$$\Delta = \left[\frac{1}{(N_\lambda - 1)} \sum_{\lambda_i=1}^{N_\lambda} \left\{ \frac{\rho_{\lambda_i}^{\text{exact}} - \rho_{\lambda_i}^{\text{acp}}}{\rho_{\lambda_i}^{\text{exact}}} \right\}^2 \right]^{1/2} \tag{14}$$

where $\rho_{\lambda_i}^{\text{exact}}$ is the exact reflectances, $\rho_{\lambda_i}^{\text{acp}}$ is computed for **K** = 1, 2, or 3, and N_λ is the number of available wavelengths, i.e., 6, since the 0.865-μm channel is used for normalization. In Figure 2 we plotted isolines of Δ in a r_m-σ plot. In Fig. 2a, where we considered the first principal component only in calculating Δ, the error Δ is generally larger than 5% and can be as large as 20% for large r_m. An interesting point that needs to be noted is that the error has a "rippled" behavior and that for some coupled values of r_m and σ the error may be quite small, less than 1%, even with one component. That means that it will be difficult to retrieve more than one parameter in such con-

Table 2. Values of Eigenvalues for the Standard Case

	Normalized Eigenvalues	Relative Contribution
First	5.95334	0.99222
Second	0.04585	0.99986
Third	0.00076	0.99999
Fourth	0.00004	1.00000
Fifth	0.00000	1.00000
Sixth	0.00000	1.00000

The aerosol refractive index is equal to 1.45 with no imaginary part, and the scattering angle is equal to 135°.

ditions. Using two components leads to an error that is always less than 5% for any values of r_m and σ (Figure 2b) and around 1% for broad size distributions ($\sigma > 0.35$) and r_m less than 1 μm. An accuracy of 1% may be achieved for any size distribution included in the database, specially for narrower distributions and larger radiuses by considering the first three components (Figure 2c). The third component may be so needed in specific conditions to supplement the first two components. That means that the new coordinates we found are not completely independent in such cases.

What is the impact of the radiometric noise? To answer this question, we use the MODIS spectral radiometric noise reported in Table 1. The error in the spectral dependence due to the radiometric noise is given by

$$\Delta^{\text{noise}} = \left[\frac{1}{(N_\lambda - 1)} \sum_{\lambda_i=1}^{N_\lambda} \left\{ \frac{Ne\Delta\rho_{\lambda_i}}{\rho_{\lambda_i}} \right\}^2 \right]^{1/2} \quad (15)$$

The Δ^{noise} values are quite similar to the isolines reported in Figure 2 and can be directly compared to them; Δ^{noise} depend on the absolute values and spectral properties of the reflectances. In Table 4, values of Δ^{noise} computed for several values of α_λ are shown. They were computed assuming that the reflectance at 865 nm is equal to 0.01. Depending on α_λ, the radiometric noise is between 3 and 10%, increasing for stronger spectral dependence. Comparing those values with the isolines in Figure 2, it is quite evident that the second component may be within the noise level and that in some specific conditions only one component needs to be used. The presence of other sources of errors (e.g., calibration or white caps) will strengthen this conclusion. The results of the present analysis depend on the reflectance value at 865 nm; for smaller reflectance values, as 0.001, one component only can be retrieved whatever the size distribution is, but reflectance of 0.01 at 865 nm is more typical and corresponds roughly to an aerosol optical thickness of 0.15. We shall discuss again that point in the error budget section.

3.3. Meaning of Components

We showed that the spectral dependence in the seven bands of MODIS of any of our aerosol models is a combination of two components. The two first principal components, which are P_l^1 and P_l^2 in (11), are plotted in Figures 3a and 3b, respectively, as a function of the wavelength in our standard case $m = 1.45$ and $\Theta = 135°$. The spectral behavior of the two components is so representative of an aerosol model that restores our 1271 spectral behaviors depending on the loadings p_n^1 and p_n^2 (equation (11)).

Let us now examine these loadings. From physical consideration the first loading p_n^1 should be related to a quantity representative of a mean angstrom exponent over the solar spectrum and the second one p_n^2 to the difference between the "visible" and the "infrared" exponents. All combinations of the spectral bands were performed and we selected the wavelengths that gave us the best correlation. The following combinations of the angstrom exponents were found to optimize the p_n^1 and p_n^2 values;

(1) the first loading p_n^1 ($\mathbf{K} = 1$) can be represented by α_{sum}

$$\alpha_{\text{sum}} = \frac{\alpha_{659}(\mu_s, \mu_v, \phi_v) + \alpha_{1240}(\mu_s, \mu_v, \phi_v)}{2} \quad (16a)$$

(2) the second loading p_n^2 ($\mathbf{K} = 2$) by α_{diff}

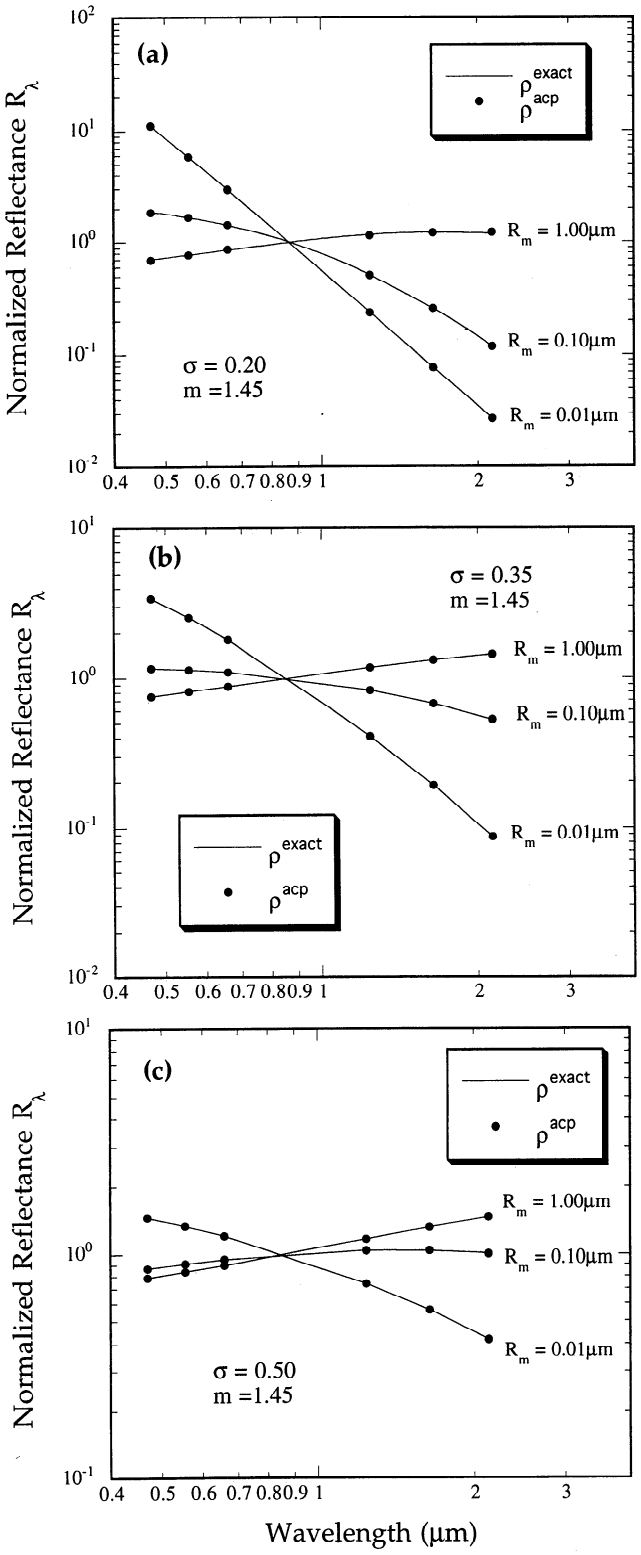

Figure 1. Normalized reflectances as a function of the wavelength for the exact reflectances ρ^{exact} and the reflectances computed from the two first components ρ^{acp} for three values of r_m (0.01, 0.10, and 1.0 μm) and a refractive index of 1.45; three values of σ have been considered: (a) $\sigma = 0.20$, (b) $\sigma = 0.35$, (c) $\sigma = 0.50$.

Table 3. Absolute Differences Between Exact Normalized Reflectances (eq (13)) and Normalized Reflectances Restored by Using Two First Components only

λ	σ = 0.20			σ = 0.35			σ = 0.50		
(μm)	0.01 μm	0.10 μm	1.00 μm	0.01 μm	0.10 μm	1.00 μm	0.01 μm	0.10 μm	1.00 μm
0.470	0.035	0.030	0.015	0.001	0.001	0.001	0.001	0.001	0.001
0.555	0.002	0.004	0.001	0.000	0.000	0.000	0.000	0.000	0.000
0.659	0.003	0.010	0.007	0.000	0.000	0.000	0.000	0.000	0.000
1.240	0.001	0.002	0.014	0.000	0.001	0.002	0.000	0.001	0.002
1.640	0.000	0.001	0.002	0.000	0.000	0.001	0.000	0.001	0.001
2.130	0.000	0.001	0.034	0.000	0.001	0.006	0.000	0.002	0.005

Three values of the median radius r_m and three values of the standard deviation σ are reported.

$$\alpha_{\text{diff}} = \alpha_{2130}(\mu_s, \mu_v, \phi_v) - \alpha_{470}(\mu_s, \mu_v, \phi_v) \quad (16b)$$

In Figures 4a and 4b we, respectively, plotted α_{sum} as a function of p_n^1 and α_{diff} as a function of p_n^2, for the same standard case, m = 1.45 and Θ = 135°. The quantities are perfectly correlated as expressed by the equations reported within the figures. Similar results are obtained for other geometric conditions and other refractive indices.

Finally, the 6×1271 angstrom coefficients can be simply written, as given in (17), for instance, at 470 nm and for the nth aerosol model,

$$\alpha_n^{470} \approx \left\{ \frac{\alpha_{659}^n + \alpha_{1240}^n}{2} \right\} \times P_{470}^1 + \{\alpha_{2130}^n - \alpha_{470}^n\} \times P_{470}^2 \quad (17)$$

The spectral information is included only in two combinations of the angstrom coefficients, α_{sum} and α_{diff}. These two quantities will be exclusively used in the next section and will be improperly named first and second components to keep in mind their meaning.

4. Inversion Scheme

The principal component analysis pointed out which spectral bands (or a combination of bands) carry information regarding the size distribution. The next step is to determine the parameters of the size distribution we can expect to retrieve with their corresponding accuracy.

4.1. Results

For a given refractive index the aerosol model is described by two independent parameters (section 2.2), the median radius r_m and the standard deviation σ of the size distribution. As the spectral dependence within the solar spectrum is expected to be restored with two principal components, the problem seems very well conditioned and the two parameters should be derived.

In Figure 5a, a plot of the second component (represented by α_{diff}) versus the first component (represented by α_{sum}) is shown for several values of r_m and σ. Three isolines are plotted by solid lines for fixed values of the standard deviation (σ = 0.20, 0.35, and 0.50) and six isolines are plotted by dotted lines for fixed values of r_m (0.001, 0.01, 0.05, 0.20, 0.50, and 1.00 μm). The scattering angle is Θ = 135° and the refractive index is 1.45°.

This figure can be used to demonstrate inversion of the aerosol size distribution from the measured spectral radiances. To illustrate it, we consider measurements with spectral properties that correspond to a first component equal to zero (α_{sum} = 0.0). From the plot in Figure 5a we have several solutions which are located on the vertical line, like {r_m = 0.50; σ = 0.20} or {r_m = 0.20;

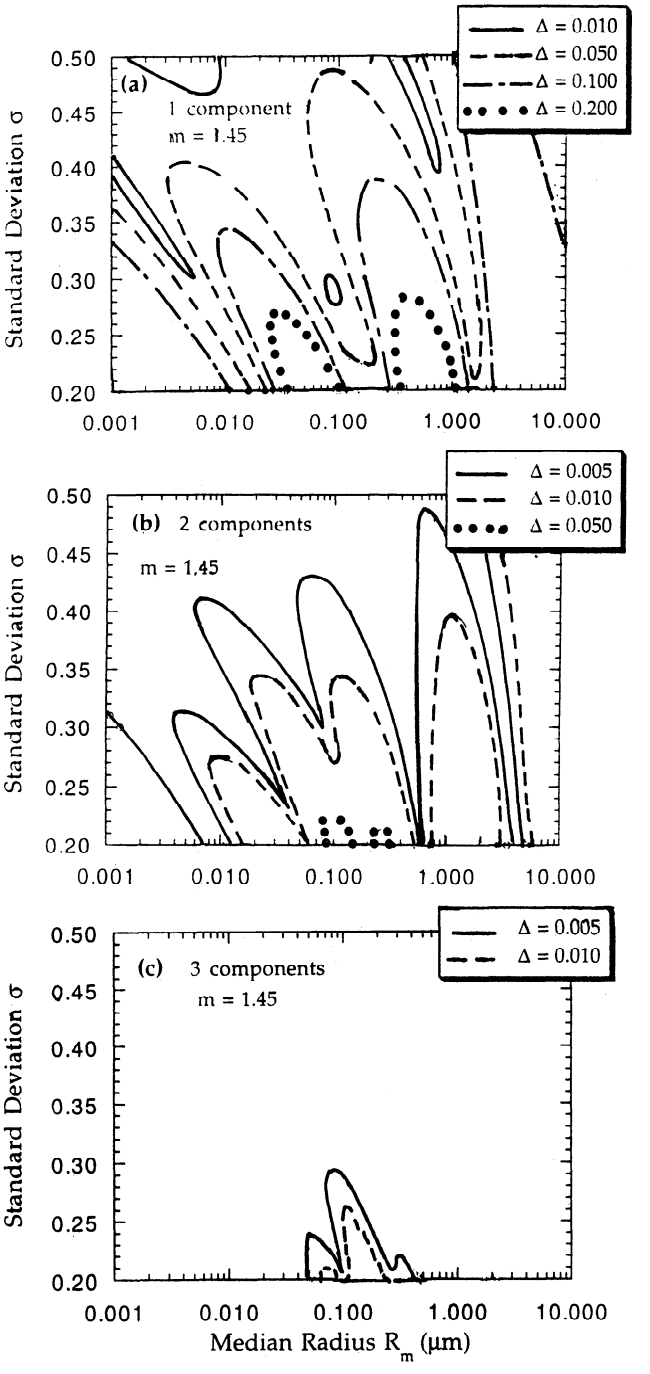

Figure 2. Isolines of the error Δ (see eq (19)) in a r_m-σ plot for several numbers of principal components: (a) 1, (b) 2, and (c) 3, respectively. The refractive index is equal to 1.45.

Table 4. Uncertainty in the Spectral Dependence of the Reflectance Due to the Sensor Radiometric Noise, As Computed by Equation (15)

α	Δ^{Noise}, Equation (15)
−2.0	0.0980
−1.5	0.0685
−1.0	0.0500
0.5	0.0393
0.0	0.0341
0.5	0.0331

The reflectance at 865 nm is 0.010.

$\sigma = 0.35\}$, or even $\{r_m = 0.05; \sigma = 0.50\}$. The second component ($\alpha_{\text{diff}}$) is then helpful to discriminate between the different solutions: a value of −1.0 corresponds to a solution of large and narrowly distributed particles ($r_m = 0.50$; $\sigma = 0.20$), while −0.3 leads to a solution of smaller particles ($r_m = 0.05$) but with a wider distribution ($\sigma = 0.50$). Similar analysis could be done for a first component α_{sum} around −2.0. However, if α_{sum} is −1.0, the previous analysis fails since the curves cross each other and there is no evidence that one solution is better than another.

The last example shows that in some cases the two parameters of the size distribution cannot be retrieved. Therefore it is worthwhile to find a single parameter that may contain most of the physical information that can be derived from the inversion. As suggested by *Van de Hulst* [1957] and extensively used by *Hansen and Hovenier* [1974], we use the optical effective radius r_{eff} defined by

$$r_{\text{eff}} = \frac{\int_0^\infty r^3 n(r)\, dr}{\int_0^\infty r^2 n(r)\, dr} \tag{18a}$$

for a lognormal size distribution, r_{eff} is given by

$$r_{\text{eff}} = r_m \exp(2.5 \ln^2 \sigma) \tag{18b}$$

leading different combinations of r_m and σ to identical values of r_{eff}.

The isolines of r_{eff} and σ in Figure 5b are closer to orthogonal than the isolines of r_m and σ, which means that r_{eff} and σ are more independent. For some values, r_{eff} isolines are almost orthogonal to α_{sum}, which means that r_{eff} is the right parameter from the first component. For example, considering the previous conditions for a first component equal to 0

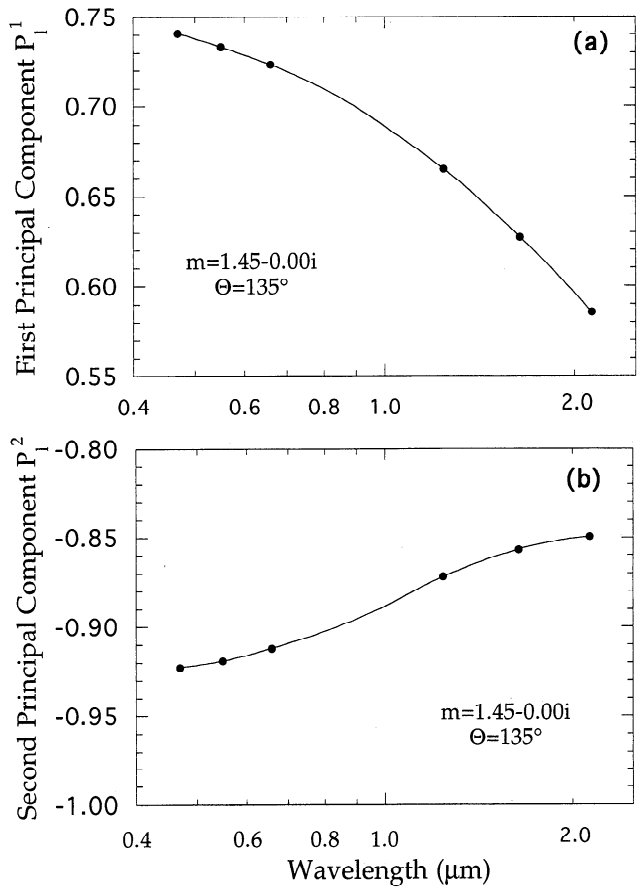

Figure 3. Principal components P_l^i as a function of the wavelength. The refractive index m is equal to 1.45. The scattering angle θ is 135°. (a) First component P_l^1, (b) second component P_l^2.

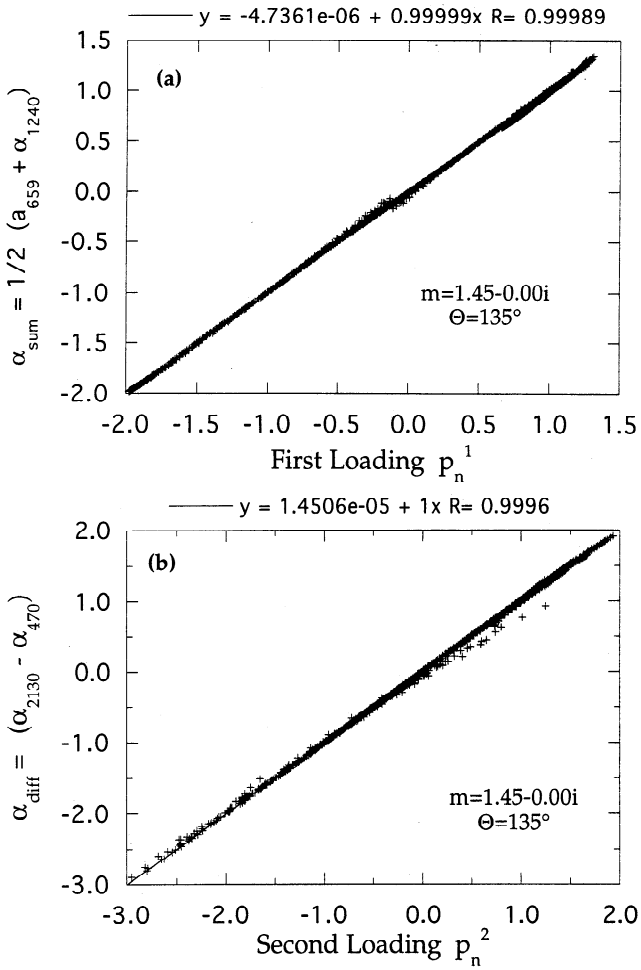

Figure 4. Correlation between the loadings p_n^i and the combinations of the angstrom exponents. The refractive index m is equal to 1.45. The scattering angle θ is 135°. (a) Correlation between the first loading p_n^1 and the mean angstrom exponent α_{sum} (see eq (16a)), (b) correlation between the second loading p_n^2 and the α_{diff} (see eq (16b)).

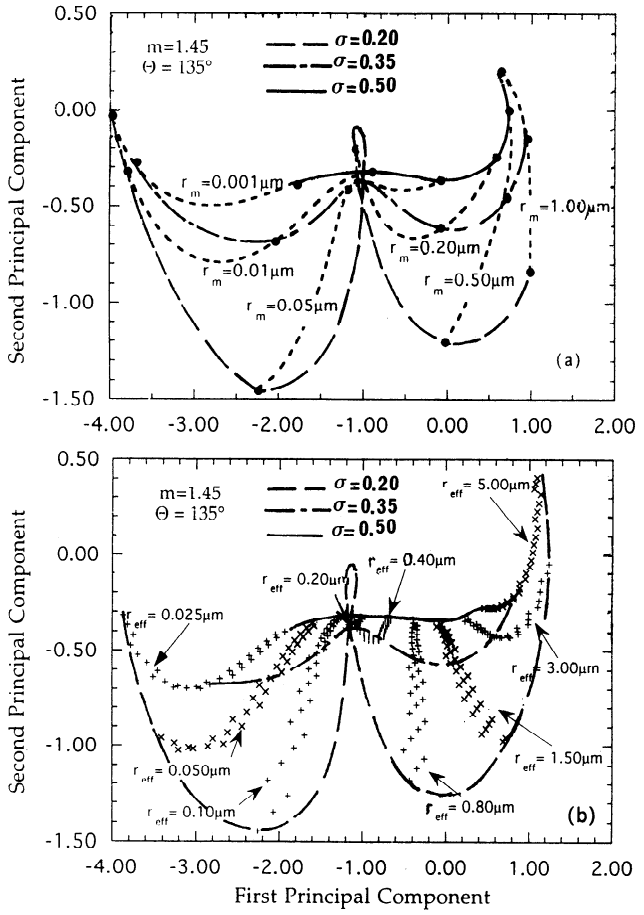

Figure 5. Contour lines of equal standard deviation σ and of equal (a) r_m and (b) r_{eff} values in a scatter diagram. The x axis corresponds to the first component (α_{sum}) and the y axis to the second component (α_{diff}). The refractive index m is equal to 1.45. The scattering angle θ is 135°. The values of σ isolines are 0.20, 0.35, and 0.50 in Figures 5a and 5b. (a) The values of r_m isolines (dashed lines) are 0.001, 0.01, 0.05, 0.20, 0.50, and 1.00 μm. The solid circles correspond to actual intersections of both isolines, other apparent intersections are not real but rather a two-dimensional display of a three-dimensional dependence. (b) The values of r_{eff} (symbols) are 0.025, 0.050, 0.10, 0.20, 0.40, 0.80, 1.50, 3.00, and 5.00 μm.

($\alpha_{\text{sum}} = 0.0$), which are not favorable conditions for inverting the size distribution, we now may derive a value of r_{eff}, between 0.8 and 1.5 μm. The discrimination is even possible by using the second component, $\alpha_{\text{diff}} \cong -0.5$ corresponding to a broad size distribution with $r_{\text{eff}} \cong 1.50$ μm; α_{diff} values around -1.0 correspond to a narrow size distribution with r_{eff} close to 0.8 μm. Values of α_{sum} around 1.0 correspond to a fairly large range of possible values of r_{eff}, between $\cong$ 1.5 and 5.0 μm; the second component may provide additional information for discrimination between particles of $r_{\text{eff}} = 1.5$ or 3.0 or larger. If the spectral measurements give $\alpha_{\text{sum}} = -1.0$, the effective radius is the only parameter we can expect to retrieve since there is no information about aerosols given by α_{diff}. Here the determination of r_{eff} can be done within a factor of 2. For smaller particles with $\alpha_{\text{sum}} = -2.0$, r_{eff} may vary by a factor of 4, between 0.025 and 0.10 μm; the second component may help us to reduce this uncertainty by a factor of 2.

Figure 6 illustrates why the spectral reflectances are less good than the spectral optical thicknesses to retrieve the aerosols size distribution. The spectral dependence of both quantities is plotted for several values of r_m and σ. Some of the reflectance curves are superimposed or cross each other (Figure 6b). On the other hand, for very large particles ($r_{\text{eff}} > 1.7$), when the optical thickness cannot provide any information, the use of reflectances may be more effective. The present results lead us to examine if there are optimum geometrical conditions for remote sensing of particle size, and if these conditions depend on the particle size being retrieved. As already pointed out by *Koepke and Quenzel* [1979], the variability of the satellite radiances with the aerosol models is depending on the view geometry.

4.2. Optimization of Geometrical Conditions

The isolines of r_{eff} are plotted for two additional scattering angles, $\Theta = 102°$ (Figure 7a) that roughly corresponds to the maximum possible forward direction while still avoiding glint effects on the sea surface, and $\Theta = 169°$ that corresponds to backward directions (Figure 7b).

It is clear from Figure 7a that scattering angles around 100° (Figure 7a) are quite well adapted for medium size particles (between 0.1 and 0.8 μm); however, these scattering angles cannot be used with sufficient confidence for larger particles. On the other hand, backscattered directions are particularly unfavorable for retrieving particles with an effective radius

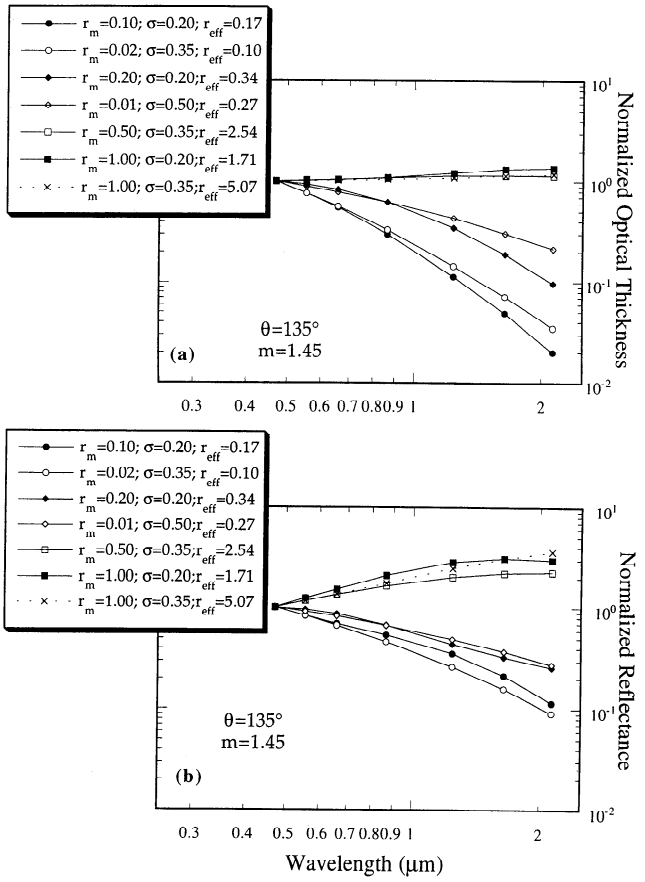

Figure 6. Spectral dependence of (a) the aerosol optical thickness and (b) the aerosol reflectance over the MODIS spectral bands for several size distributions. The normalization is done at 470 nm for the purpose of clarity. The refractive index m is equal to 1.45. The scattering angle θ is 135°.

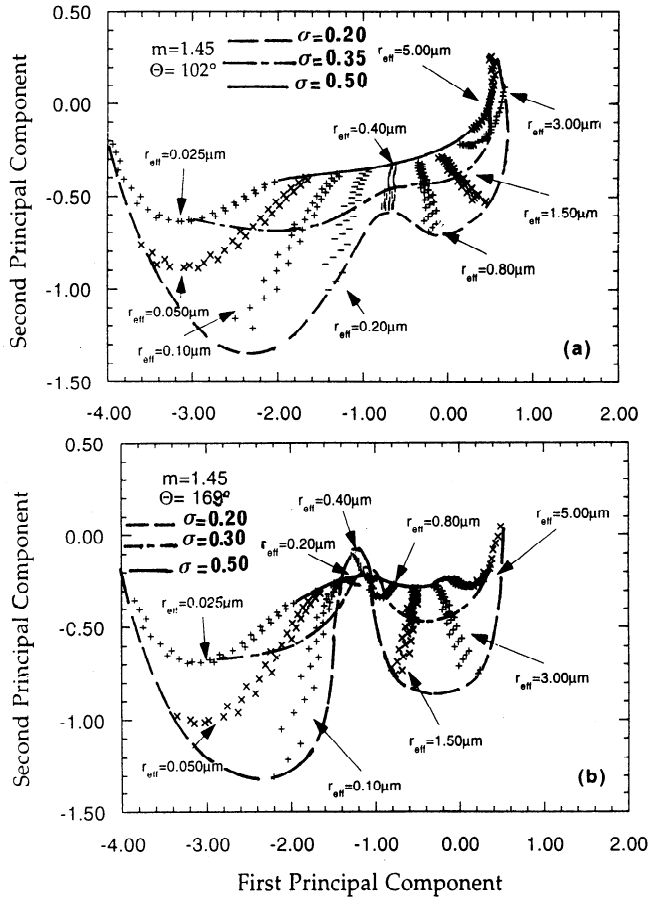

Figure 7. Contour lines of equal standard deviation σ and of equal r_{eff} values in a scatter diagram. The x axis corresponds to the first component (α_{sum}) and the y axis to the second component (α_{diff}). The refractive index m is equal to 1.45. The scattering angle θ is 135°. The values of σ isolines are 0.20, 0.35, and 0.50. The values of r_{eff} (symbols) are 0.025, 0.050, 0.10, 0.20, 0.40, 0.80, 1.50, 3.00, and 5.00 μm. (a) For a scattering angle equal to Θ = 102°, (b) for a scattering angle equal to Θ = 169°.

between 0.2 and 0.8 μm, but they are quite suitable for large particles $r_{eff} > 1.5$ μm. Previous conclusions for very small particles are unchanged.

As the expected size distributions over ocean correspond to medium size particles, the retrieval will be better performed for scattering angles around 100° but with the constraint of avoiding the glint. Depending on the geometrical conditions, the size distribution, by use of r_{eff} and of the standard deviation σ for some specific conditions, can be retrieved within a factor of 2. The accuracy can be different when instrumental noise is considered, as shown in the next section.

4.3. Error Budget

The radiometric noise has an impact on the aerosol size distribution retrieval. The retrieval is also sensitive to errors in the absolute and spectral calibration, but these are not considered in the present analysis. We computed the errors $\Delta\alpha$ on the angstrom exponent as deduced from the spectral reflectances by

$$\Delta\alpha_\lambda = -\frac{1}{\ln\left(\frac{\lambda}{865}\right)}\left\{\left(\frac{\Delta\rho_\lambda}{\rho^a_\lambda}\right)^2 + \left(\frac{\Delta\rho_{865}}{\rho^a_{865}}\right)^2\right\}^{1/2} \quad (19)$$

where the errors $\Delta\rho_\lambda$ are due to the radiometric noise of the MODIS instrument (Table 1). The results are reported in Table 5 for a typical reflectance at 865 nm, $\rho^a_{865} = 0.01$. The resulting errors in the two principal components are given by

$$\Delta\alpha_{sum} = \{(\Delta\alpha_{659})^2 + (\Delta\alpha_{1240})^2\}^{1/2} \quad (20a)$$

$$\Delta\alpha_{diff} = \{(\Delta\alpha_{470})^2 + (\Delta\alpha_{2130})^2\}^{1/2} \quad (20b)$$

Values of the radiometric noise given in Table 5 are the nominal values and can be reduced by deriving the size distribution from an average of an array of pixels. A 5 km × 5 km resolution, i.e., 100 MODIS pixels, is a good compromise. If the cloud cover is 70% in average, we still have 30 pixels within the box which are cloud free. As the algorithm rejects the third of the pixels that are the brightest for ensuring a perfect cloud screening and the third that are the darkest for the possible associated shadows, there are, on average, 10 available pixels for retrieval and the errors in Table 5 may be reduced by a factor of 3. These reduced errors are the values that we use in this section. To illustrate the impact of the radiometric noise on the retrieval, we also considered additional values of the reflectance at 865 nm, 0.002, and 0.050 that correspond to extremely clean and turbid conditions, respectively.

The results of Figure 7a are plotted again in Figure 8a in a different way. For several values of r_{eff} (0.05, 0.10, 0.20, 0.40, 0.80, and 1.50 μm) we plotted the whole range of possible values of α_{sum}, by straight lines that reasonably correspond to extreme values of σ with some overlapping between them. A small extent means that α_{sum} is quite independent of the standard deviation (the effective radius is the only independent parameter); a large extent means that for the same value of the effective radius, α_{sum} is quite dependent of σ. Overlapping between the ranges for several values of r_{eff} means that the effective radius is not accurately determined by using α_{sum} only. For instance, a value of $\alpha_{sum} = -0.70$ indicates that the effective radius is quite well determined ($r_{eff} = 0.40$ μm) independently of σ; a value of $\alpha_{sum} = -1.40$ indicates that the effective radius may be 0.10 μm with a broad size distribution ($\sigma = 0.50$) or 0.20 μm with a very narrow size distribution ($\sigma = 0.20$). If the radiometric noise is not considered, the retrieval

Table 5. Errors (Absolute Values As Expressed in Equations (19) and (20)) in Spectral Angstrom Exponents and in Two First Components Due to MODIS Radiometric Noise

	$\Delta\alpha_{470}$	$\Delta\alpha_{550}$	$\Delta\alpha_{659}$	$\Delta\alpha_{1240}$	$\Delta\alpha_{1640}$	$\Delta\alpha_{2130}$	$\Delta\alpha_{sum}$	$\Delta\alpha_{diff}$
$\alpha = -2.00$	0.022	0.042	0.112	0.289	0.303	0.338	0.310	0.339
$\alpha = -1.00$	0.041	0.065	0.147	0.202	0.160	0.137	0.249	0.143
$\alpha = 0.00$	0.076	0.102	0.192	0.141	0.084	0.056	0.238	0.094
$\alpha = 1.00$	0.140	0.159	0.253	0.098	0.044	0.023	0.271	0.141

Four spectral dependencies are considered. The reflectance at 865 nm is 0.010.

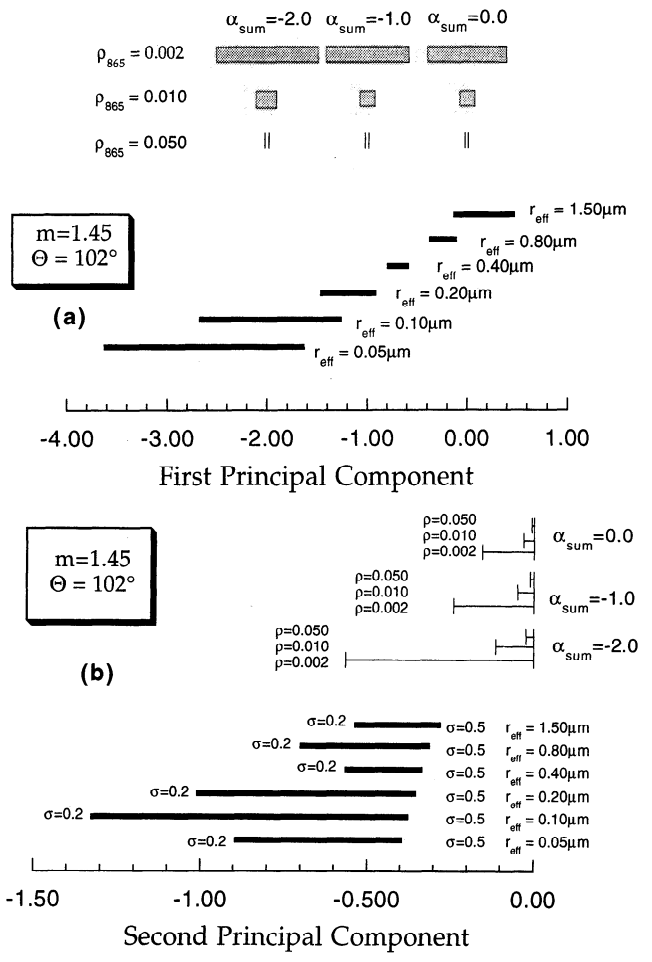

Figure 8. Length of the first and second components for different effective radiuses. The refractive index m is equal to 1.45. The scattering angle θ is 102°. (a) Corresponds to the first component α_{sum}; the dashed boxes correspond to the errors for three values of α_{sum} and three values of ρ_{865}. (b) Corresponds to the second component α_{diff}; the dashed boxes have been replaced by solid lines.

of the effective radius is well performed for particle size between 0.2 and 0.8 μm. The dashed boxes reported at the top of Figure 8a show the errors $\Delta\alpha_{sum}$ due to radiometric noise. Note that the error is not very dependent on the size of the particles since the extent of the boxes are similar for the three values of α_{sum}. For medium turbidity conditions (ρ_{865} = 0.010) an accurate inversion can be performed, though not so accurate as for ρ_{865} = 0.050. For very clean conditions the size distribution cannot be retrieved since the wide range of the dashed boxes for ρ_{865} = 0.002 almost completely masks the effect of particle size.

We performed a similar study for α_{diff} (Figure 8b). Here the extent of the error bars is more dependent on α_{sum} values since the error is twice larger for −2.0 than for −1.0. Once the value of r_{eff} is determined from α_{sum}, the second component may be used to discriminate between narrow and broad aerosol size distributions; the accuracy of the retrieval of σ depends on the r_{eff} values. The second component is useless for getting any additional information on the effective radius; for very broad size distribution (σ = 0.5), α_{diff} varies between −0.4 and −0.3 only (which is the uncertainty resulting from the radiometric noise for medium turbidity conditions), when r_{eff} varies between 0.05 and 1.50 μm. In summary, the second component can bring additional information on the width of the size distribution as long as the turbidity conditions are not too low.

4.4. Impact of the Refractive Index

The refractive index of the particles adds additional uncertainty in the retrieval scheme since its value is not precisely known. To estimate the impact, we compare the two components, α_{sum} and α_{diff}, for several values of the real (m_r) and imaginary parts (m_i) of m.

In Figures 9a and 9b we plotted the difference between α_{sum} and α_{diff} for m = 1.45 and 1.40, as a function of the effective radius, for three values of Θ = 169°, 135°, and 102°. It is interesting to notice that again, the optimum geometrical condition (Θ = 102°) is less affected by the value of the refractive index. It is still true for larger uncertainties on m_r (1.55 and 1.45 in Figure 10) although the resulting errors become significant. It may perturb the retrieval since the corresponding error is comparable to the radiometric noise for medium turbidity conditions. The imaginary part has no impact on the retrieval (Figure 11) as long as particles are small (r_{eff} < 0.1 μm). If

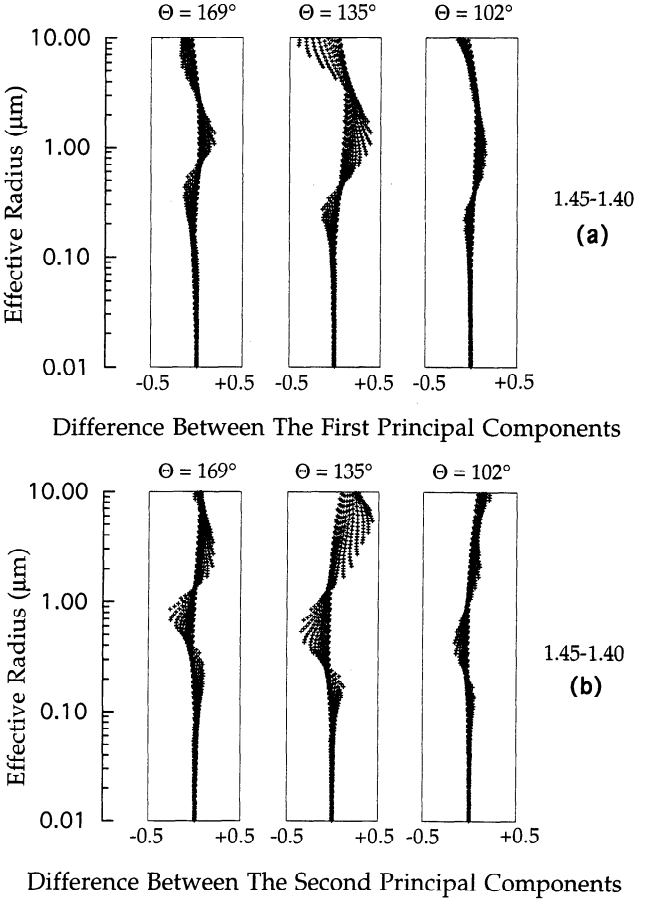

Figure 9. Differences between the first and the second components computed for two refractive indices, 1.45 and 1.40, as a function of the effective radius, r_{eff}. The reference case is m = 1.40. Each plus corresponds to one of the 1271 size distributions. Three geometrical conditions are considered: θ = 102°, 135°, and 169°. (a) Corresponds to the first component α_{sum}, (b) corresponds to the second component α_{diff}.

particles are larger ($r_{eff} \approx 1.0$ μm), the impact is still negligible when they are not very absorbing ($m_i \leq -0.02$).

5. Discussion

We used several assumptions in the present sensitivity study: (1) the aerosol size distribution is represented by a single mode following a lognormal distribution; (2) there is no account for errors resulting from the extraction of the aerosol signal from the satellite data; and (3) particles are assumed to be spherical. In addition, all the computations were performed assuming that the single-scattering approximation is valid. The impact of these assumptions is briefly examined in the following section, but it may require an additional study that will be given in a forthcoming paper.

5.1. Bimodal Size Distribution

The aerosol model was described with a single lognormal, while a bimodal aerosol model might be more representative of the actual conditions. Assuming that there are two modes with a fixed mode of small particles that corresponds to the accumulation mode, we performed a sensitivity study for different radiuses of the second mode considering the following simplifications: (1) the two modes have the same standard deviations and (2) the refractive index is the same for the two modes ($m = 1.45\text{-}0.000i$). The scattering angle of 102° was selected.

The resulting size distribution can be written

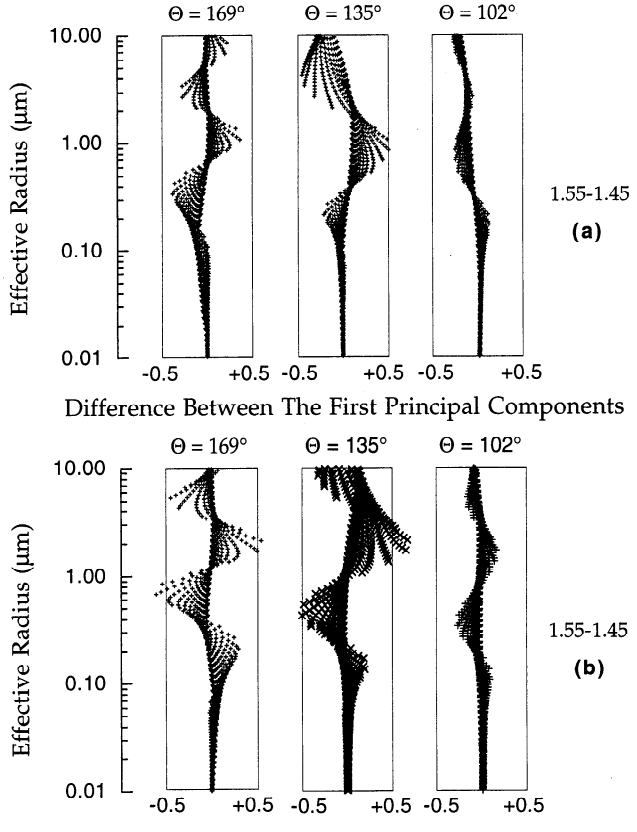

Figure 10. Same as in Figure 9 except m = 1.55 and 1.45. The reference case is $m = 1.45$.

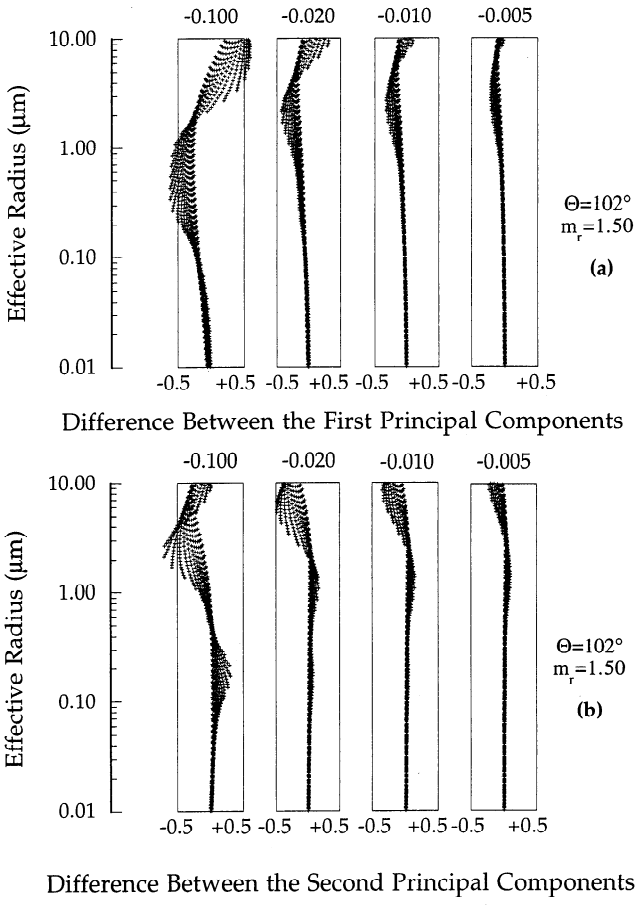

Figure 11. Differences between the first and the second components computed for different imaginary parts of the refractive index, −0.005, −0.010, −0.20, and −0.100, as a function of the effective radius, r_{eff}. The reference case is m = 1.50-0.000i. Each plus corresponds to one of the 1271 size distributions. The scattering angle θ is 102°. (a) Corresponds to the first component α_{sum}, (b) corresponds to the second component α_{diff}.

$$n(r) = \frac{dN(r)}{dr} = \sum_{j=1}^{2} \frac{dN_j(r)}{dr} \tag{21a}$$

where $dN_j(r)/dr$ is given by (3); that is,

$$\frac{dN_j(r)}{dr} = \frac{N_j}{(2\pi)^{1/2}\sigma_j 2.3r} \exp\left\{-\frac{(\log r - \log r_{m_j})^2}{2\sigma_j^2}\right\} \tag{21b}$$

with $\sigma_1 = \sigma_2 = 0.30$. The median radius of the first mode r_{m_1} is equal to 0.05 μm; the radius of the second mode r_{m_2} varies between 0.05 and 10.0 μm.

The mixing of the two modes is performed by weighting the optical properties as an external mixing; reflectances are still computed using single-scattering approximation. The density number N_j of each mode is computed for different values of the ratio of reflectances at 865 nm; that is,

$$R = \frac{\rho_{865}^{(\text{mode1})}}{\rho_{865}^{(\text{mode1})} + \rho_{865}^{(\text{mode2})}} \tag{22}$$

the total density number ($N = N_1 + N_2$) corresponds to 1 particle per volume unit. Therefore $R = 0.90$ means that 90% of the reflectance at 865 nm is provided by the first mode.

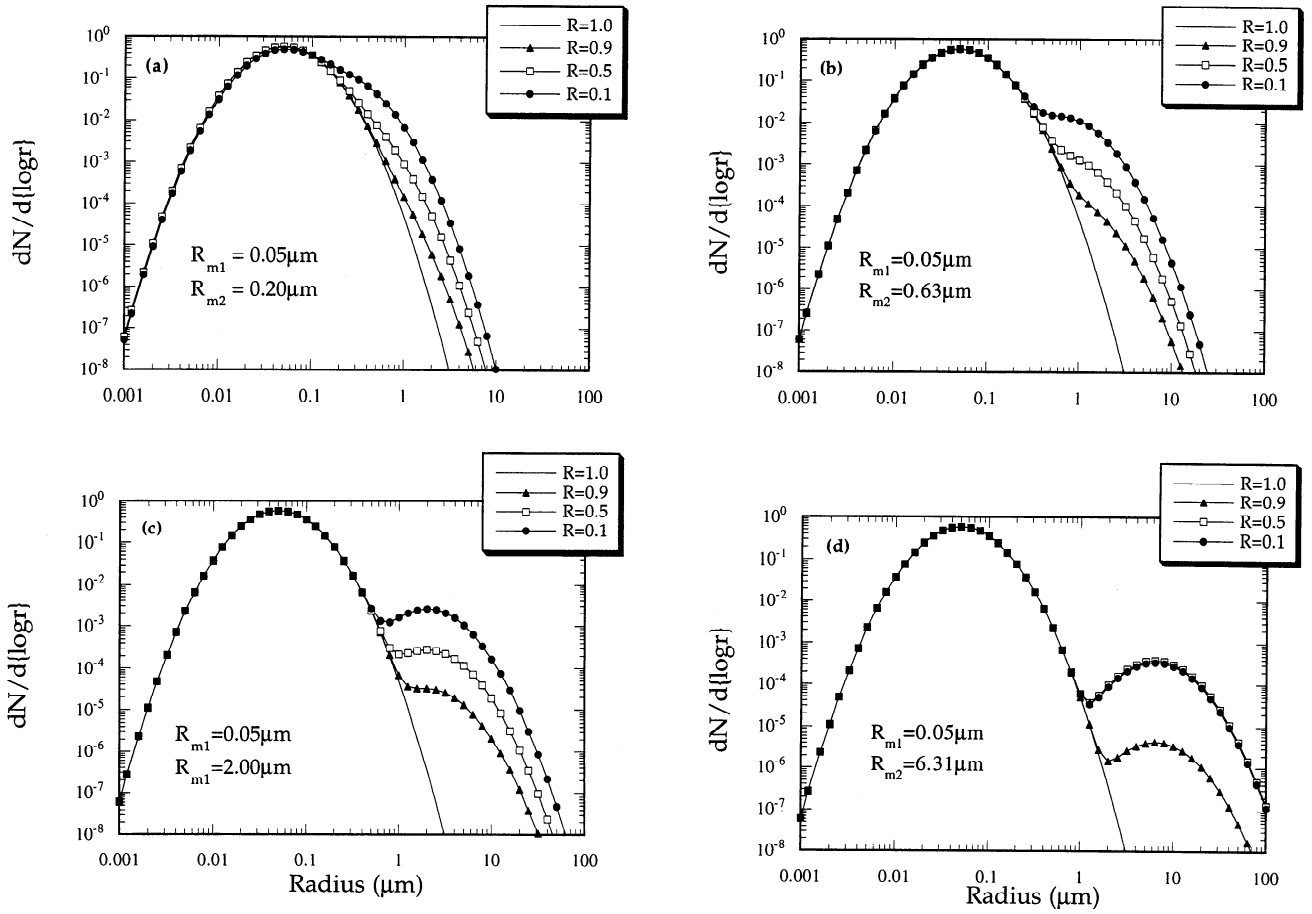

Figure 12. Aerosol size distribution for different R ratios. The median radius of the first mode is 0.05 μm; the second mode is centered at (a) 0.20 μm, (b) 0.63 μm, (c) 2.00 μm, and (d) 6.31 μm, respectively. The standard deviation is σ = 0.30 for the two modes.

Four values of r_{m_2} (0.20, 0.63, 2.00, and 6.3 μm) and four values of R (1.0, 0.9, 0.5, and 0.1) were selected. The corresponding size distributions are reported in Figure 12. The spectral reflectances $\rho_{\lambda i}^{\text{bimod}}$ were computed for several combinations of the selected values of r_{m_2} and R: R = 0.10 for (1) r_{m_2} = 0.20 μm, (2) r_{m_2} = 0.63 μm, and (3) r_{m_2} = 2.00 μm, then R = 0.90 for (4) r_{m_2} = 6.30 μm; α_{sum} and α_{diff} are plotted in Figure 13 as a function of r_{m_2} for the three values of R: 0.9, 0.5, and 0.1; the arrows correspond to the selected cases. Cases (2) and (3) give the same α_{sum} (Figure 13a) but different values of α_{diff} (Figure 13b). Obviously, case (1) corresponds to a size distribution very similar to the single mode (Figure 12a), while case (4) corresponds to a strong bimodal size distribution (Figure 12d) but with a comparable α_{sum} value (Figure 13a).

When the first mode is contributing up to 90% of the total reflectance, the first component (Figure 13a) is not very affected by the presence of the second mode; it varies between -1.28 and -1.07 only. The second component depends more on the radius of the second mode since it varies between -0.7 and -0.25. For R equal to 0.5 and 0.10, the first component is affected as soon as r_{m_2} is larger than 0.10 μm. On the contrary, the second components are quite similar for both values of R. The presence of a second mode sufficiently affects the spectral reflectances; the visible and infrared slopes are different even for R = 0.90.

The goal is now to see if there is any single-mode size distribution that can restore the spectral behavior given by two modes. So, the algorithm using single modes is applied to the spectral reflectances $\rho_{\lambda i}^{\text{bimod}}$. The single size distributions have to be passed by the following tests:

$$\delta\alpha_{\text{sum}} = \text{Abs}\{\alpha_{\text{sum}}^{\text{bimod}} - \alpha_{\text{sum}}^{\text{sing}}\} < 0.10 \qquad (23a)$$

$$\delta\alpha_{\text{diff}} = Abs\{\alpha_{\text{diff}}^{\text{bimod}} - \alpha_{\text{diff}}^{\text{sing}}\} < 0.05 \qquad (23b)$$

where the threshold values, 0.10 and 0.05, have been chosen to correspond to the radiometric noise given in Table 5, assuming there are 10 perfectly clear pixels within a box of 10×10 pixels. The threshold $\delta\alpha_{\text{diff}}$ = 0.05 is slightly overestimated for $\alpha = -2.00$, but our selection of input size distributions mostly corresponds to α values between -1 and 0.

Several solutions passed both tests, but only the size distribution that minimizes the quantity

$$\varepsilon = [\{\delta\alpha_{\text{sum}}\}^2 + \{\delta\alpha_{\text{diff}}\}^2]^{1/2} \qquad (24)$$

is reported in Figures 14–17.

Figure 14 shows case (1). As expected, the spectral dependence is not sufficiently affected and a single mode with r_m = 0.125 μm and a standard deviation σ = 0.34 perfectly restores the spectral dependence. Cases (2) and (3) are a good illustration of the utility of α_{diff} since it allows to retrieve two

different single-mode size distributions for identical values of α_{sum} (Figures 15 and 16). More surprising are the results in Figure 17 since a single equivalent size distribution corresponding to very small particles $r_m = 0.0063$ μm with a very large standard deviation gives a quite similar spectral behavior.

These results confirm the difficulty of getting the right solution since the shape of the actual size distribution does not put sufficient constraint on the reflectances over the MODIS spectral range. In addition, there would be several solutions in our database that would give the right spectral variations, as reported in Figure 18. For cases (1), (3), and (4), ε was computed for all the single size distributions included in the database and plotted as a function of r_{eff}. Clearly, the solution is not unique since there is no real information for ε values less than 10^{-1}. Nevertheless, cases (1) and (3) give a rather sharp function, which allows an accurate determination of r_{eff}; case (4) gives a broader distribution of possible r_{eff} values. It means that the retrieved values are consistent although they do not correspond to the input value.

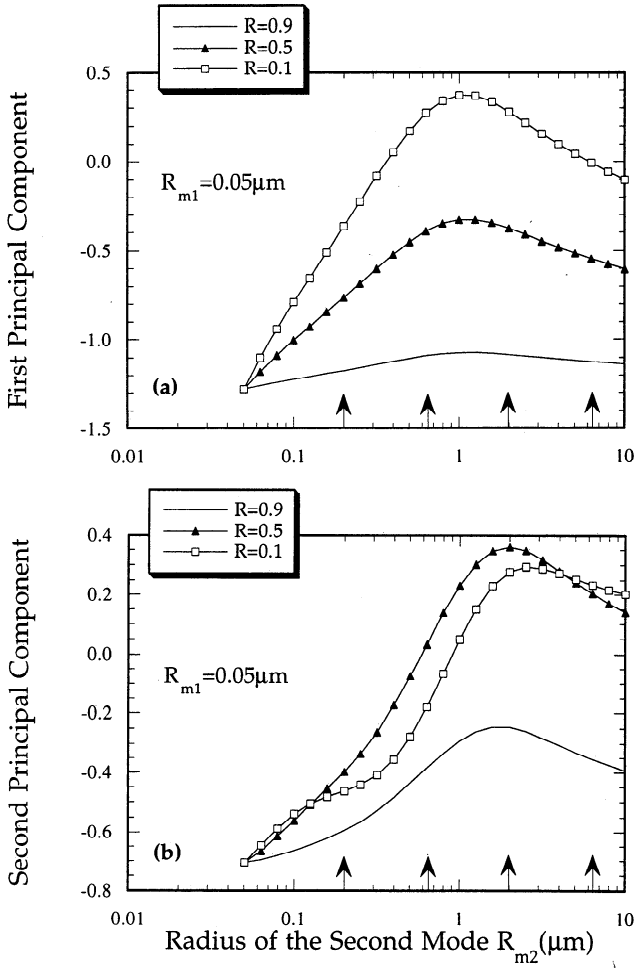

Figure 13. First and second components as a function of the median radius r_{m_2} of the second mode. The median radius r_{m_1} of the first mode is 0.05 μm. Both modes have the same standard deviation, $\sigma = 0.30$. Three ratios are considered: $R = 0.90$, 0.50, and 0.10; $R = 0.90$ means that 90% of the reflectance at 865 nm is provided by the first mode. (a) Corresponds to the first component α_{sum}, (b) corresponds to the second component α_{diff}.

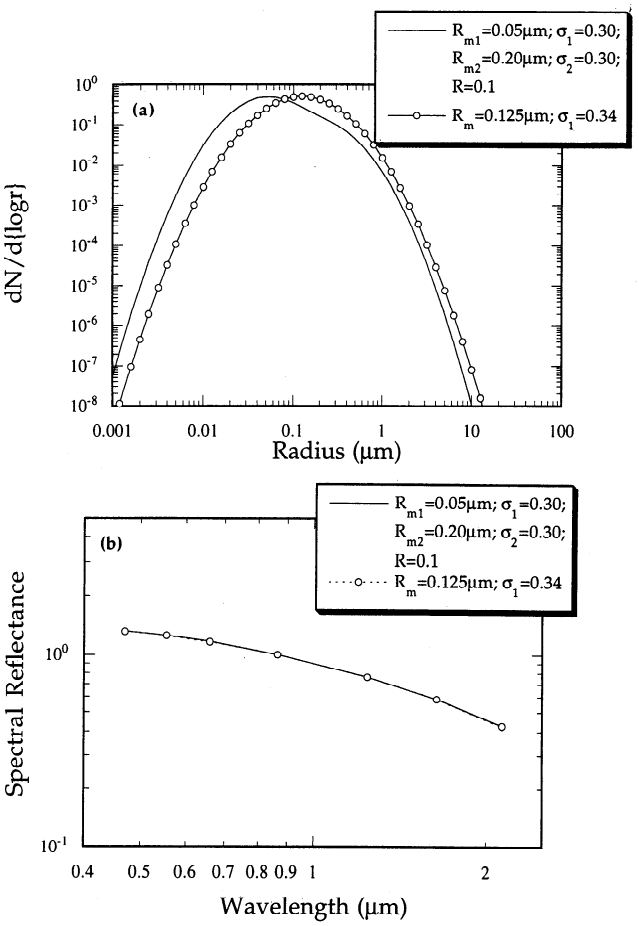

Figure 14. (a) Size distribution of the bimodal model (lines) used in the simulation compared to the size distribution of the single mode (circles) which restores the spectral reflectances. (b) Simulated (lines) and restored (circles) spectral reflectances. The input size distribution is defined by $r_{m_1} = 0.05$ μm, $r_{m_2} = 0.20$ μm, and $R = 0.10$. The refractive index m is equal to 1.45. The scattering angle θ is 102°.

5.2. Extraction of the Aerosol Signal

There are several contributions to the satellite signal: photons scattered by aerosols particles and molecules, photons transmitted or scattered by the atmosphere, reflected by the ocean and transmitted or scattered again through the atmosphere to the sensor. The Fresnel ocean surface reflectance [*Cox and Munk*, 1954], reflectance due to chlorophyll pigments, and sediments within the water [*Morel and Prieur*, 1977; Gordon 1979], and the reflectance of white caps or foam [*Whitlock et al.*, 1982; *Koepke*, 1984] are perturbing terms that have to be subtracted for getting the atmospheric component. Then, the molecular (or Rayleigh) scattering has to be removed for extracting the aerosol spectral reflectances. As the different contributions are spectrally dependent, some channels might be more suitable than others. For instance, although the blue channel (470 nm) is very attractive since it corresponds to the shortest wavelength, it is very contaminated by ocean reflectance and the additional information it provides, as compared to the 550 channel, may be lost because of the larger noise level. In addition, there is a coupling term between molecules and aerosol scattering at 470 nm [*Deschamps et al.*, 1983] which makes the extraction of the aerosols signal even more difficult.

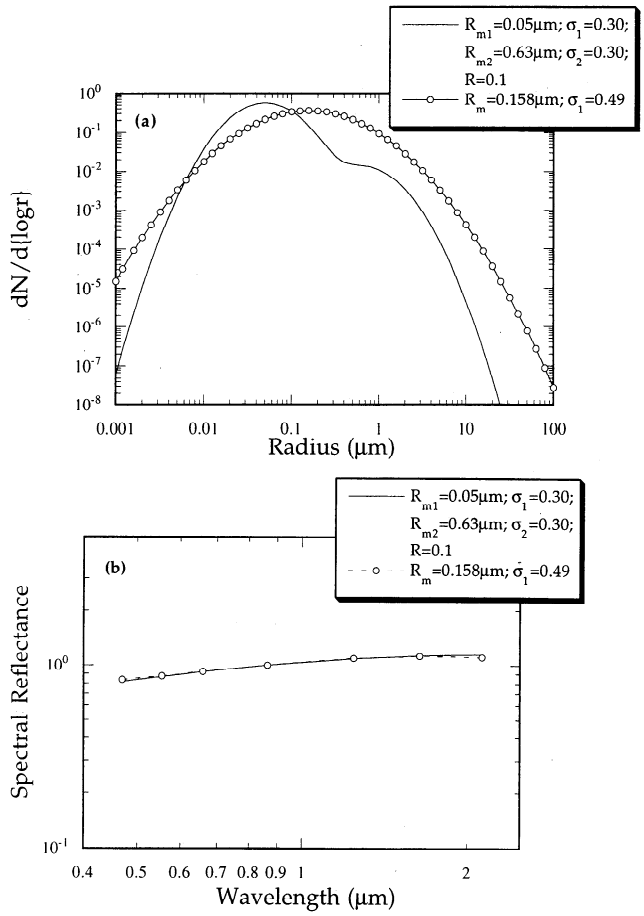

Figure 15. Same as in Figure 14 except for $r_{m_2} = 0.63$ μm.

Regardless, the order of magnitude of the errors in each spectral band involved in the extraction, the impact of dropping wavelengths from the data set used in the retrieval, is shown in Figure 19; α_{diff} is plotted versus α_{sum} for several values of the two parameters r_{eff} and σ in a similar way than in Figure 7a where bands 659 and 1240 nm were used for computing α_{sum} and bands 470 and 2130 nm for computing α_{diff}. In Figure 19a, α_{diff} is computed from bands 550 and 2130 nm, in Figure 19b from bands 659 and 2130 nm; α_{sum} is still, in both cases, computed from the 659- and 1240-nm bands. In Figure 19c all the visible bands are dropped; α_{sum} is computed from the 1240-nm band only and α_{diff} from bands 1240 and 2130 nm. The scattering angle is $\Theta = 102°$ and the refractive index is equal to 1.45.

Clearly, the blue channel, contaminated by uncertainties in underwater reflectance and multiple scattering, is not crucial and can be dropped due to the small differences observed between Figures 7a and 19a. On the other hand, by reducing too much, the spectral information leads to an ill-conditioned problem; σ and r_{eff} isolines are less and less orthogonal when the spectral information is reduced (Figure 19b). It is quite obvious in Figure 19c that the second component becomes useless when the visible information is suppressed.

As a conclusion, the selection of the channels has to be optimized and may depend on the expected quality of the ocean water. It is well known, for instance, that coastal zones are very turbid, which affects the reflectance at 670 nm, and in these regions it might be better not to use this channel. To make a definitive statement, more accurate simulations of the reflectances of the ocean-atmosphere system are needed.

5.3. Sphericity of Particles

The aerosol optical properties are presently described with the use of the Mie theory that is applicable to spherical particles only. Recent studies [*Mishchenko and Travis*, 1993] showed that the impact of the particles shape may be important for the polarized light. *Wiscombe and Mugnai* [1988] showed that the side-scattering region (θ = 80°-160°) is strongly affected by nonsphericity. *Koepke and Hess* [1988] pointed out that scattering angle of 120°, which is close to our optimal geometrical conditions, is the angle that is the most affected by particles shape in the desert aerosol case. A detailed theoretical study can be found in a recent paper by *Mishchenko and Travis* [1994].

As nonsphericity occurs for dry particles, we believe that the aerosol particles over the ocean have more probabilities to be spherical. In addition, we believe that the spectral dependence should not be much different comparing with equivalent spheres, but the question still needs to be addressed. Even if we are confident in the retrieved size parameters, we should be concerned by the determination of the aerosol optical thickness that can be strongly affected by the nonsphericity effects on the phase function computation [*Mishchenko et al.*, 1995].

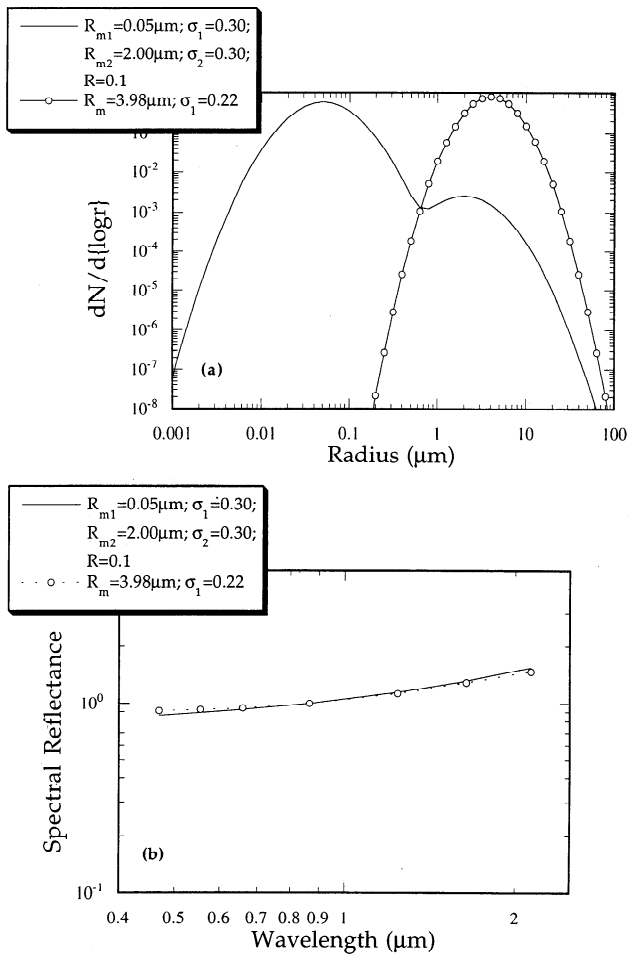

Figure 16. Same as in Figure 14 except for $r_{m_2} = 2.00$ μm.

5.4. Multiple Scattering

The study has been performed according to the single-scattering approximation. A complete analysis with multiple-scattering considerations is out the scope of this paper, but a general statement can be made. From a previous study devoted to aerosol retrievals from AVHRR channels, *Kaufman et al.* [1990] showed that the same value of the angstrom coefficient may correspond to several combinations of the standard deviation and of the effective radius in the single-scattering approximation. However, they also showed that the nonuniqueness is eliminated by the multiple scattering that results in a smoothing of the phase function effect. So, it confirms that, depending on the geometric conditions, it is difficult to retrieve more than one parameter, although it is better determined.

6. Conclusion

Information on the aerosol size distribution contained in the reflected solar spectral radiances detected over the oceans can be reduced into two quantities: (1) a mean angstrom exponent computed over the 659-nm and the 1240-nm bands and (2) the difference between the near-infrared (2130 nm) and the visible (470 nm) angstrom exponents. These quantities have been determined in an unbiased way with the use of the principal components. Consequently, only one to two parameters of the size distribution can be retrieved. For a single mode distribution these parameters are the effective radius of the particles and the width of the size distribution. The accuracy of the retrieval depends on the view and illumination directions. For example, particles with radius of 0.2 to 0.4 μm will be better retrieved for a scattering angle of 100°. The backscattered directions are more sensitive to larger particles. Accurate knowledge of the refractive index, real and imaginary parts, is not critically important for the retrieval as long as the retrieved particles are smaller than 1.0 μm. This result also holds better for scattering angles around 100°. An error budget shows that very clean conditions are not suitable for getting any information on the aerosol size distribution.

A surprising result of this investigation is that the spectral reflectance of a bimodal-lognormal distribution can be simulated very well with spectral reflectance of a single lognormal with an appropriate radius and width of distribution, σ, that do not necessary correspond to an average of the bimodal values. The present results change drastically our philosophy regarding the retrieval scheme. In the analysis of MODIS data we shall be forced to assume that after correction for stratospheric aerosol the size distribution is described by two lognormal modes: an accumulation mode (sulfates or organic particles, including smoke) and a large-particle mode of maritime particles and/or dust. The main retrieved parameter, in addition to the retrieval of the total spectral optical thickness, will then be the ratio of the volumes of the two modes. Careful simulations of the inversion procedure for MODIS in the presence of instrumental and natural sources of errors will show if additional information can be retrieved. Present simulations (see Figures 5b, 7a, and 7b) indicate that with an accurate determination of the second component and for optimum geometry conditions, it may be possible to distinguish if the accumulation mode is composed mainly of small particles associated with gas phase processes ($r_{\text{eff}} \sim 0.1$ μm) or particles associated with in-cloud processes ($r_{\text{eff}} \sim 0.2$ μm). Alternatively, it may be possible to distinguish if the large particles are mainly of maritime origin ($r_{\text{eff}} \sim 0.8$-1.5 μm) or dust ($r_{\text{eff}} \sim 2$-3 μm). A

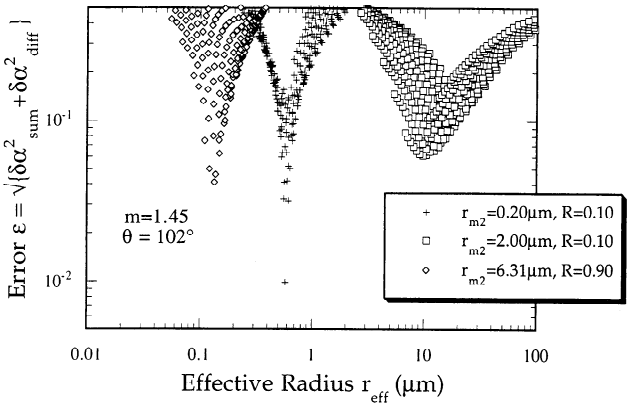

Figure 18. Errors $\varepsilon = [\{\delta\alpha_{sum}\}^2 + \{\delta\alpha_{diff}\}^2]^{1/2}$ as a function of the effective radius; $\delta\alpha_{sum}$ (respectively $\delta\alpha_{diff}$) are the differences between the α_{sum} values (respectively α_{diff}) provided by the bimodal size distribution and the values given by the single lognormal size distributions. Three different bimodal size distributions are considered: plus, $r_{m_2} = 0.20$ μm and $R = 0.10$; square, $r_{m_2} = 2.00$ μm and $R = 0.10$; diamond, $r_{m_2} = 6.31$ μm and $R = 0.90$. The refractive index m is equal to 1.45. The scattering angle θ is 102°.

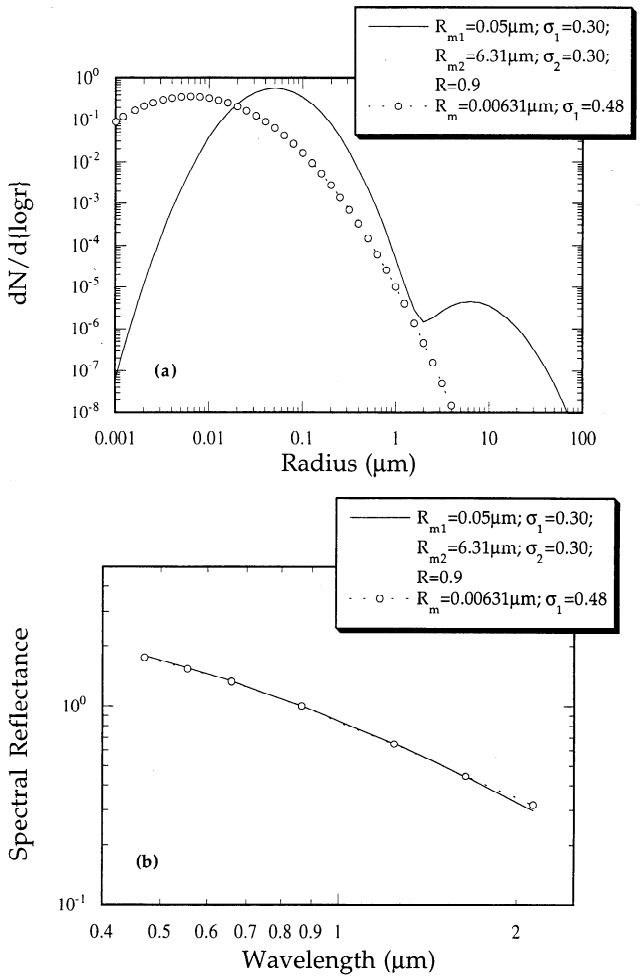

Figure 17. Same as in Figure 14 except for $r_{m_2} = 6.31$ μm and $R = 0.90$.

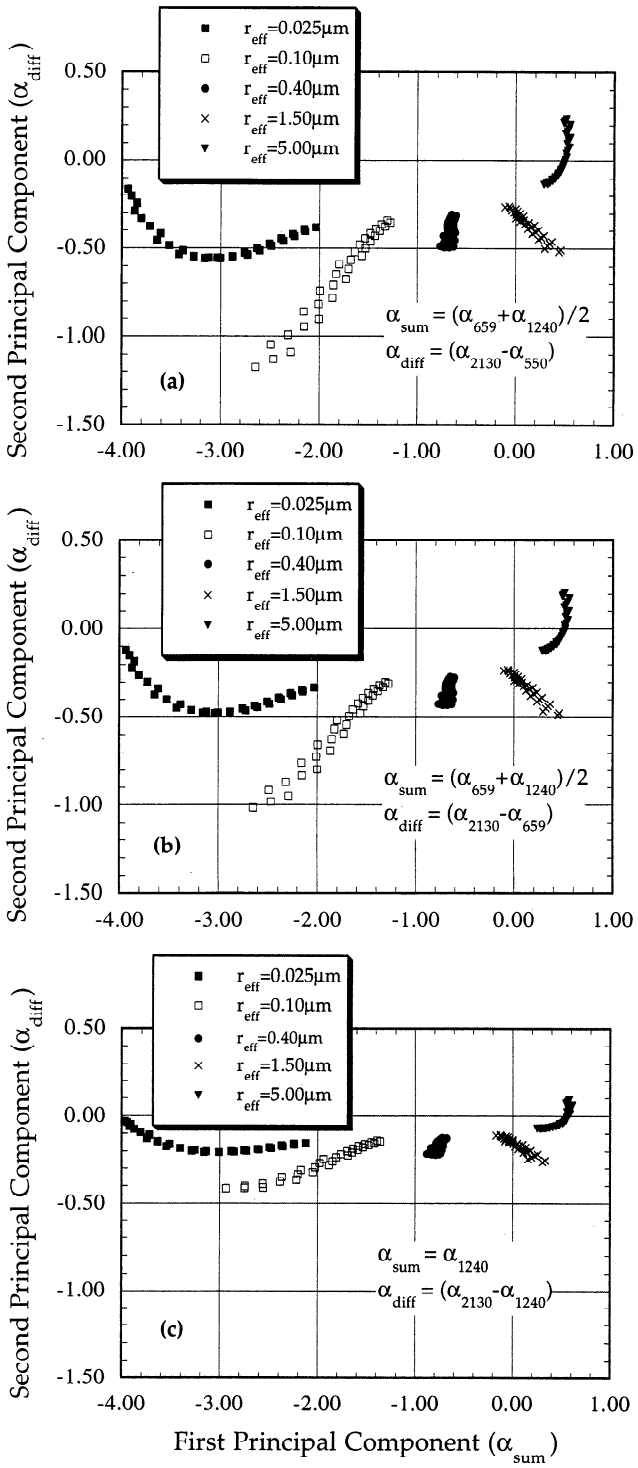

Figure 19. Sensitivity of the retrieval to the extend of the spectral range. Plots of equal r_{eff} values in a scatter diagram. The x axis corresponds to the first component (α_{sum}) and the y axis to the second component (α_{diff}). Values of r_{eff} are 0.025, 0.10, 0.40, 1.50, and 5.00 μm. The refractive index m is equal to 1.45. The scattering angle θ is 102°. (a) The spectral range is [550–2130 nm], so $\alpha_{sum} = (\alpha_{659} + \alpha_{1240})/2$ and $\alpha_{diff} = \alpha_{2130} - \alpha_{550}$. (b) The spectral range is [659–2130 nm], so $\alpha_{sum} = (\alpha_{659} + \alpha_{1240})/2$ and $\alpha_{diff} = \alpha_{2130} - \alpha_{659}$. (c) The spectral range is [865–2130 nm], so $\alpha_{sum} = (\alpha_{1240})$ and $\alpha_{diff} = \alpha_{2130} - \alpha_{1240}$.

detailed size distribution of the atmospheric aerosol will rather be derived from a global network of ground-based instruments for remote sensing of Sun and sky radiation [*Tanré et al.*, 1988b; *Nakajima et al.*, 1989; *Kaufman et al.*, 1994; *Holben et al.*, 1994; *Kaufman and Holben*, 1996]. To the best of our knowledge, no such detailed investigations of the information content of polarization or angular properties of the reflected light were performed. These approaches may be more informative than the spectral radiance and may overcome the deficiencies of the present algorithm.

The lack of sensitivity of the spectral reflected radiance to details of the aerosol size distribution is probably also the reason for the relative success in corrections of remote sensing of oceanic phytoplankton for contamination by aerosol scattering [*Gordon*, 1978; *Morel and Gordon*, 1980]. In such corrections, a short spectral range of the reflected light (e.g., 660-750 nm) is used to predict the atmospheric path radiance at shorter wavelengths (down to 410 nm). A more complex dependence of the spectral radiance on the aerosol size distribution would have prohibited this type of extrapolation.

Acknowledgments. This study has been funded by NASA (National Aeronautics and Space Administration) under the EOS program and by CNES (Centre National d'Etudes Spatiales), the French Space Agency. One of us (DT) would like to thank USRA for its support and the Climate and Radiation Branch in GSFC/NASA for its kind hospitality. The LOA is sponsored by CNRS (Centre National de la Recherche Scientifique).

References

Albrecht, B. A., Aerosols, cloud microphysics and fractional cloudiness, *Science*, *245*, 1227–1230, 1989.

Andrea, M. O., and W. R. Barnard, The marine chemistry of dimethylsulfide, *Mar. Chem.*, *14*, 267–279, 1984.

Artaxo, P., F. Gerab, M. A. Yamasoe, and J. V. Martins, Fine mode aerosol composition at three long-term atmospheric monitoring sites in the Amazon Basin, *J. Geophys. Res.*, *99*, 22,857–22,868, 1994.

Benkovitz, C. M., C. M. Berkowitz, R. C. Easter, S. Nemesure, R. Wagener, and S. E. Schwartz, Sulfate over the North Atlantic and adjacent continental regions: Evaluation of October and November 1986 using a three-dimensional model driven by observation-derived meteorology, *J. Geophys. Res.*, *99*, 20,725–20,756, 1994.

Carlson, T. N., Atmospheric turbidity in Saharan dust outbreaks as determined by analyses of satellite brightness data, *Mon. Weather Rev.*, *107*, 322–335, 1979.

Chahine, M. T., A general relaxation method for inverse solution of the full radiative transfer equation, *J. Atmos. Sci.*, *29*, 741–747, 1972.

Charlson, R. J., J. E. Lovelock, M. O. Andreae, and S. G. Warren, Oceanic phytoplankton, atmospheric sulphur, cloud albedo and climate, *Nature*, *326*, 655–661, 1987.

Charlson, R. J., S. E. Schwartz, J. M. Hales, R. D. Cess, J. A. Coackley Jr., J. E. Hansen, and D. J. Hofman, Climate forcing of anthropogenic aerosols, *Science*, *255*, 423–430, 1992.

Coakley, J. A., Jr., and R. D. Cess, Response of the NCAR community climate model to the radiative forcing by the naturally occurring tropospheric aerosols, *J. Atmos. Sci.*, *42*, 1677–1692, 1985.

Coakley, J. A., Jr., R. D. Cess, and F. B. Yurevich, The effect of tropospheric aerosol on the earth's radiation budget: A parameterization for climate models, *J. Atmos. Sci.*, *40*, 116–138, 1983.

Coakley, J. A., Jr., R. L. Borstein, and P. A. Durkee, Effect of ship stack effluents on cloud reflectance, *Science*, *237*, 953–1084, 1987.

Cox, C., and W. Munk, Statistics of the sea surface derived from sun glitter, *J. Mar. Res.*, *13*, 198–208, 1954.

Crutzen, P. J., Atmospheric interaction—Homogeneous gas reactions of C, N, and S containing compounds, in *The Major Biogeochemical Cycles and Their Interactions*, edited by B. Bolin and R. B. Cook, pp. 67–114, John Wiley, New York, 1983.

d'Almeida, G. A., P. Koepke, and E. P. Shettle, *Atmospheric Aerosols, Global Climatology and Radiative Chasracteristics*, A. Deepak, Hampton, Va., 1991.

Deschamps, P. Y., M. Herman, and D. Tanré, Modeling of the atmospheric effects and its application to the remote sensing of ocean color, *Appl. Opt.*, *22*, 3751–3758, 1983.

Deschamps, P. Y., F. M. Bréon, M. Leroy, A. Podaire, A. Bricaud, J. C. Buricz, and G. Sèze, The POLDER mission: Instrument characteristics and scientifics objectives, *IEEE Trans. Geosci. Remote Sens.*, *32*, 598–615, 1994.

Deuzé, J. L., F. M. Bréon, P. Y. Deschamps, C. Devaux, M. Herman, A. Podaire, and J. L. Roujean, Analysis of the POLDER (Polarization and Directionality of Earth's Reflectances) airborne instrument, *Remote Sens. Environ.*, *45*, 137–154, 1993.

Diner, D. J., et al., MISR, A multiangle imaging spectroradiometer for geophysical and climatological research from EOS, *IEEE Trans. Geosci. Remote Sens.*, *27*, 200–214, 1989.

Duce, R. A., Biogeochemical cycles and the air-sea exchange of aerosols, in *The Major Biogeochemical Cycles and Their Interactions*, edited by B. Bolin and R. B. Cook, John Wiley, New York, 1983.

Dulac, F., D. Tanré, G. Bergametti, P. Buat-Menard, M. Desbois, and D. Sutton, Assessment of the African airborne dust mass over the western Mediterranean Sea using Meteosat data, *J. Geophys. Res.*, *97*, 2489–2506, 1992.

Durkee, P. A., Aerosol characteristics with dual wavelength radiance measurements, in *Preprints of 2nd Conference on Satellite Meteorology, Remote Sensing and Applications*, Am. Meteorol. Soc., Boston, Mass., 1985.

Fairall, C. W., K. L. Davidson, and G. E. Schacher, An analysis of the surface production of sea-salt aerosols, *Tellus*, *35B*, 31–39, 1983.

Ferrare, R. A., R. S. Fraser, and Y. J. Kaufman, Satellite remote sensing of large-scale air pollution: Measurements of forest fires smoke, *J. Geophys. Res.*, *95*, 9911–9925, 1990.

Fraser, R. S., Satellite measurement of mass of Saharan dust in the atmosphere, *Appl. Opt.*, *15*, 2471–2479, 1976.

Fraser, R. S., Y. J. Kaufman, and R. L. Mahoney, Satellite measurements of aerosol mass and transport, *Atmos. Environ.*, *18*, 2577–2584, 1984.

Gordon, H. R., Removal of atmospheric effects from satellite imagery of the oceans, *Appl. Opt.*, *17*, 1631–1636, 1978.

Gordon, H. R., Diffuse reflectance of the ocean: The theory of its augmentation by chlorophyll *a* fluorescence at 685 nm, *Appl. Opt.*, *18*, 1161–1166, 1979.

Griggs, M., Measurements of atmospheric aerosol optical thickness over water using ERTS-1 data, *J. Air Pollut. Control Assoc.*, *25*, 622–626, 1975.

Griggs, M., Satellite observations of atmospheric aerosols during the EOMET cruise, *J. Atmos. Sci.*, *36*, 695–698, 1979.

Hansen, J. E., and J. W. Hovenier, Interpretation of the polarization of Venus, *J. Atmos. Sci.*, *31*, 1137–1160, 1974.

Hansen, J. E., and A. A. Lacis, Sun and dust versus greenhouse gases: An assessment of their relative roles in global climate change, *Nature*, *346*, 713–719, 1990.

Heathershaw, A. D., Bursting phenomena in the sea, *Nature*, *248*, 394–395, 1974.

Hegg, D. A., Heterogeneous production of cloud condensation nuclei in the marine atmosphere, *Geophys. Res. Lett.*, *17*, 2165–2188, 1990.

Hegg, D. A., R. J. Ferek, and P. V. Hobbs, Aerosol size distribution in the cloudy atmospheric boundary layer of the North Atlantic Ocean, *J. Geophys. Res.*, *98*, 8841–8846, 1993.

Hobbs, P. V., and J. D. Locatelli, Ice nucleus measurements at three sites in western Washington, *J. Atmos. Sci.*, *27*, 90–100, 1970.

Holben, B. N., E. Vermote, Y. J. Kaufman, D. Tanré, and V. Kalb, Aerosols retrieval over land from AVHRR data—Application for atmospheric correction, *IEEE Trans. Geosci. Remote Sens.*, *30*, 212–222, 1992.

Holben, B. N., T. F. Eck, I. Slutsker, A. Setzer, A. Pereira, E. Vermote, J. A. Reagan, Y. J. Kaufman, and D. Tanré, Sunphotometer network measurement of aerosol properties in the Brazilian Amazon, paper presented at Val d'Isere Conference on Physical Measurements and Signatures in Remote Sensing, ISPRS, January 17–21, 1994.

Hoppel, W. A., J. W. Fitzgeral, G. M. Frick, R. E. Larson, and E. J. Mack, Aerosol size distribution and optical properties found in the marine boundary layer over the Atlantic Ocean, *J. Geophys. Res.*, *95*, 3659–3686, 1990.

Intergovernmental Panel on Climate Change (IPCC), *Radiative Forcing of Climate Change*, edited by B. Bolin, J. Houghton, and L. G. M. Filho, UNEP, World Meteorol. Organ., Geneva, 1994.

Ishimaru, A., R. J. MarksII, L. Tsang, C. M. Lam, and D. C. Park, Particle-size distribution determination using optical sensing and neural networks, *Opt. Lett.*, *15*, 1221–1223., 1990.

Jaenicke, R., and L. Schütz, Comprehensive study of physical and chemical properties of the surface aerosols in the Cape Verde Islands region, *J. Geophys. Res.*, *83*, 3585–3599, 1978.

Jankowiak, I., and D. Tanré, Climatology of Saharan dust events observed from Meteosat imagery over Atlantic Ocean, Method and preliminary results, *J. Clim.*, *5*, 646–656, 1992.

Joseph, J. H., The sensitivity of a numerical model of the global atmosphere to the presence of desert aerosol, in *Aerosols and Their Climatic Effects*, edited by H. E. Gerber and A. Deepak, pp. 215–226, A. Deepak, Hampton, Va., 1984.

Junge, C. E., *Air Chemistry and Radioactivity*, 374 pp., Academic, San Diego, Calif., 1963.

Kaufman, Y. J., and B. N. Holben, Hemispherical backscattering by biomass burning and sulfate particles derived from sky measurements, *J. Geophys. Res.*, in press, 1996.

Kaufman, Y. J., and T. Nakajima, Effect of Amazon smoke on cloud microphysics and albedo—Analysis from satellite imagery, *J. Appl. Meteorol.*, *32*, 729–744, 1993.

Kaufman, Y. J., and C. Sendra, Algorithms for atmospheric corrections of visible and near IR satellite imagery, *Int. J. Remote Sens.*, *9*, 1357–1381, 1988.

Kaufman, Y. J., and D. Tanré, Effect of variations in supersaturation on the formation of cloud condensation nuclei, *Nature.*, *369*, 45–48, 1994.

Kaufman, Y. J., R. S. Fraser, and R. A. Ferrare, Satellite measurements of large-scale air pollution methods, *J. Geophys. Res.*, *95*, 9895–9909, 1990.

Kaufman, Y. J., R. S. Fraser, and R. L. Mahoney, Fossil fuel and biomass burning effect on climate-Heating or cooling?, *J. Clim.*, *4*, 578–588, 1991.

Kaufman, Y. J., A. Gitelson, A. Karnieli, E. Ganor, R. S. Fraser, T. Nakajima, S. Mattoo, and B. N. Holben, Size distribution and phase function of aerosol particles retrieved from sky brightness measurements, *J. Geophys. Res.*, *99*, 10,341–10,356, 1994.

King, M. D., Sensitivity of constrained linear inversions to the selection of the Lagrange multiplier, *J. Atmos. Sci.*, *39*, 1356–1369, 1982.

King, M. D., D. M. Byrne, B. M. Herman, and J. A. Reagan, Aerosol size distribution obtained by inversion of optical depth measurements, *J. Atmos. Sci.*, *35*, 2153–2167, 1978.

King, M. D., Y. Kaufman, P. Menzel, and D. Tanré, Remote sensing of cloud, aerosol and water vapor properties from the moderate resolution imaging spectrometer (MODIS), *IEEE Trans. Geosci. Remote Sens.*, *30*, 2–27, 1992.

Koepke, P., Effective reflectance of oceanic whitecaps, *Appl. Opt.*, *23*, 1816–1823, 1984.

Koepke, P., and M. Hess, Scattering functions of tropospheric aerosols: The effects of nonspherical particles, *Appl. Opt.*, *27*, 2422–2430, 1988.

Koepke, P., and H. Quenzel, Turbidity of the atmosphere determined from satellite calculation of optimum viewing geometry, *J. Geophys. Res.*, *84*, 7847–7855, 1979.

Langner, J., and H. Rodhe, A global three dimensional model of the tropospheric sulfur cycle, *J. Atmos. Chem.*, *13*, 225–263, 1991.

Liou, K. N., K. P. Freeman, and T. Sasamori, Cloud and aerosol effects on the solar heating rate of the atmosphere, *Tellus*, *30*, 62–70, 1978.

Martonchik, J. V., and D. J. Diner, Retrieval of aerosol optical properties from multi-angle satellite imagery, *IEEE Trans. Geosci. Remote Sens.*, *30*, 223–230, 1992.

Mateer, C. L., On the information content of Umkehr observations, *J. Atmos. Sci.*, *28*, 370–381, 1965.

Mekler, Y., H. Quenzel, G. Ohring, and I. Marcus, Relative atmospheric aerosol content from ERTS observations, *J. Geophys. Res.*, *82*, 967–972, 1977.

Mishchenko, M. I., and L. D. Travis, Light scattering by polydisperse, rotationally symmetric nonspherical particles: Linear polarization, *J. Quant. Spectrosc. Radiat. Transfer*, *51*, 759–778, 1993.

Mishchenko, M. I., and L. D. Travis, Light scattering by polydispersions of randomly oriented spheroids with sizes comparable to wavelengths of observation, *Appl. Opt.*, *33*, 7206–7225, 1994.

Mishchenko, M. I., and L. D. Travis, Nonsphericity of dust-like tropospheric aerosols: Implications for aerosol remote sensing and climate modeling, *Geophys. Res. Lett.*, *22*, 1077–1080, 1995.

Morel, A., and L. Prieur, Analysis of variations in ocean color, *Limnol. Oceanogr.*, *22*, 709–722, 1977.

Morel, A., and H. R. Gordon, Report of the working group on water color, *Boundary Layer Meteorol.*, *18*, 177–182, 1980.

Nakajima, T., M. Tanaka, M. Yamano, M. Shiobara, K. Arao, and Y. Nakanishi, Aerosol optical characteristics in the yellow sand events observed in May, 1982 at Nagasaki, 2, Models, *J. Meteorol. Soc. Jpn.*, *67*, 279–291, 1989.

Norton, C. C., F. R. Mosher, B. Hinton, D. W. Martin, D. Santek, and W. Kuhlow, A model for calculating desert aerosol turbidity over oceans from geostationary satellite data, *J. Appl. Meteorol.*, *19*, 633–642, 1980.

Novakov, T., and J. E. Penner, Large contribution of organic aerosols to CCN concentration, *Nature*, *365*, 823–826, 1993.

Penner, J. E., R. E. Dickinson, and C. A. O'Neill, Effects of aerosol from biomass burning on the global radiation budget, *Science*, *256*, 1432–1434, 1992.

Prospero, J. M., Eolian transport to the world ocean, in *The sea*, vol. 7, *The Oceanic Lithosphere*, edited by C. Emiliani, pp. 801–874, John Wiley, New York, 1981.

Pye, K., *Aeolian Dust and Dust Deposit*, 335 pp., Academic, San Diego, Calif., 1987.

Radke, L. F., J. A. Coakley Jr., and M. D. King, Direct and remote sensing observations of the effects of ships on clouds, *Science*, *246*, 1146–1148, 1989.

Rao, C. R. N., E. P. McClain, and L. L. Stowe, Remote-sensing of aerosols over the oceans using AVHRR data theory, practice and applications, *Int. J. Remote Sens.*, *10*, 743–749, 1989.

Rivera-Carpio, C. A., C. E. Corrigan, T. Novakov, J. E. Penner, C. F. Rogers, and J. C. Chow, Derivation of contributions of sulfate and carbonaceous aerosol to cloud condensation nuclei from mass size distributions, *J. Geophys. Res.*, in press, 1996.

Rodgers, C. D., Retrieval of atmospheric temperature and composition from remote measurements of thermal radiation, *Rev. Geophys.*, *14*, 609–624, 1976.

Salomonson, V. V., W. L. Barnes, P. W. Maymon, H. E. Montgomery, and H. Ostrow, MODIS: Advanced facility instrument for studies of the Earth as a system, *IEEE Trans. Geosci. Remote Sens.*, *27*, 145–153, 1989.

Santer, R., and M. Herman, Particle size distribution from forward scattered light using the Chahine inversion scheme, *Appl. Opt.*, *22*, 2294–2302, 1983.

Shettle, E. P., and R. W. Fenn, Models for the aerosol of the lower atmosphere and the effect of humidity variations on their optical properties, *AFGL Tech. Rep.*, *AFGL-TR 790214*, Air Force Geophys. Lab., Hanscom AFB, Maine, 1979.

Tanré, D., J. F. Geleyn, and J. Slingo, First results of the introduction of an advanced aerosol-radiation interaction in ECMWF low resolution global model, in *Aerosols and Their Climatic Effects*, edited by H. E. Gerber and A. Deepak, pp. 133–177, A. Deepak, Hampton, Va., 1984.

Tanré, D., P. Y. Deschamps, C. Devaux, and M. Herman, Estimation of Saharan aerosol optical thickness from blurring effects in thematic mapper data, *J. Geophys. Res.*, 15,955–15,964, 1988a.

Tanré, D., C. Devaux, M. Herman, R. Santer, and J. Y. Gac, Radiative properties of desert aerosols by optical ground-based measurements at solar wavelengths, *J. Geophys. Res.*, *83*, 14,223–14,231, 1988b.

Taylor, G. S., M. B. Baker, and R. J. Charlson, Heterogeneous interactions of the C, N and S cycles in the atmosphere: The role of aerosols and clouds, in *The Major Biogeochemical Cycles and their Interactions*, B. Bolin and R. B. Cook, John Wiley, New York, 1983.

Travis, L. D., *EOSP: Earth Observing Scanning Polarimeter*, EOS reference handbook 1993, edited by G. Asrar and D. J. Dokken, pp. 74–75, NASA, 1993.

Twitty, J. T., The inversion of aureole measurements to derive aerosol size distribution, *J. Atmos. Sci.*, *32*, 584–591, 1975.

Twomey, S. A., The influence of pollution on the short wave albedo of clouds, *J. Atmos. Sci.*, *34*, 1149–1152, 1977a.

Twomey, S. A., Introduction to the mathematics of inversion in remote sensing and indirect measurements, in *Developments in Geomathematics*, vol. 3, 243 pp., Elsevier Sci., New York, 1977b.

Twomey, S. A., and J. Warner, Comparison of measurements of cloud droplets and cloud nuclei, *J. Atmos. Sci.*, *24*, 702–703, 1967.

Twomey, S. A., M. Piepgrass, and T. L. Wolfe, An assessment of the impact of pollution on the global albedo, *Tellus*, *36B*, 356–366, 1984.

Van de Hulst, H. V., *Light Scattering by Small Particles*, John Wiley, New York, 1957. (Reprinted in 1981 by Dover, Mineola, New York).

Whitby, K. Y., The physical characteristics of sulfur aerosols, *Atmos. Environ.*, *12*, 135–159, 1978.

Whitlock, C. H., D. S. Bartlett, and E. A. Gurganus, Sea foam reflectance and influence on optimum wavelength for remote sensing of ocean aerosols, *Geophys. Res. Lett.*, *9*, 719–722, 1982.

Wigley, T. M. L., Possible climate change due to SO_2 derived cloud condensation nuclei, *Nature*, *339*, 355–357, 1989.

Wiscombe, W. J., and A. Mugnai, Scattering from nonspherical Chebyshev particles, 2, Means of angular scattering patterns, *Appl. Opt.*, *27*, 2405–2421, 1988.

M. Herman and D. Tanré (corresponding author) Laboratoire d'Optique Atmosphérique, Centre National de la Recherche Scientifique et Université des Sciences et Technologies de Lille - Bat P5, 59655, Villeneuve d'Ascq, France.

Y. J. Kaufman, Laboratory for Atmospheres, NASA GSFC, Code 913, Greenbelt, MD 20771.

(Received May 18, 1995; revised December 19, 1995; accepted December 19, 1995.)